
Pro gradu -tutkielma
Fysiikan suuntautumisvaihtoehto

# MELT POND COVERAGE AND TEMPORAL EVOLUTION AT DRIFTING STATION TARA DURING SUMMER 2007

Paula Sankelo

Huhtikuu 2008

Ohjaajat: Dos. Jari Haapala, prof. emer. Seppo Manninen

Tarkastajat: Dos. Jari Haapala, prof. emer. Seppo Manninen

HELSINGIN YLIOPISTO
FYSIKAALISTEN TIETEIDEN LAITOS

PL 64 (Gustaf Hällströmin katu 2)
00014 Helsingin yliopisto

# Table of Contents

# 1. Introduction

Sea ice albedo is one of the key parameters in climate system. When temperatures rise in the summer, sea ice and the snow on top of it start melting. Melt pond formation lowers the regional surface albedo of sea ice, because water has a significantly lower albedo than either snow or ice. As the surface albedo of sea ice diminishes, even more short-wave radiation is absorbed in the ice. This further enhances the melting, which again lowers the regional albedo. This process is called the sea ice-albedo feedback mechanism, and it is suspected to amplify climate warming in the polar regions. Conversely, a downward trend in global temperature would increase the sea ice albedo, which would then accelerate the cooling. (Curry 1995; Curry 2001.)

In its very simplest form, sea-ice albedo feedback mechanism is thought to operate by the decreasing of snow- and ice-covered areas as a result of warming. The less ice and snow there is, the smaller portion of incoming solar radiation is reflected from the surface. However, it has been shown by different sea-ice models that sea-ice albedo feedback operates on multi-year ice as well. Even if an ice floe survives the melting season, it will respond to the increase in summer temperatures. Curry et. al. (1995) have looked into the internal transformation processes which contribute to the sea ice-albedo feedback on multi-year ice. Such processes include the melting of snow cover, diminishing of total ice thickness, opening of leads and formation of melt ponds in the summer. (Curry et. al. 1995.)

It is clear that the amount of melt ponds markedly affects sea ice albedo: the surface albedo of sea ice is the lowest, when the areal fraction of melt ponds is the greatest. When modelling the sea-ice albedo feedback and its climatic effects, it is important to have reliable data on melt pond coverage on the Arctic sea ice. However, it doesn't

ultimately serve modelling purposes to know the melt pond coverage as an input parameter only. To correctly incorporate the sea ice-albedo feedback into the climate models, one must also know the physical processes involved that govern melt pond formation. The behaviour of the sea ice-albedo feedback can be reliably simulated only if the correct physical dependencies are included in the model. The processes that control melt pond formation must also be coupled with other physical processes and climatic factors within the model, just as they are in reality. (Curry et. al. 1995; Curry et. al. 2001.)

In order to accumulate the kind of data needed for accurate sea ice-albedo modelling, it is necessary to observe the sea ice melt processes for long periods of time. The temporal scale of sea ice albedo studies should optimally cover at least a full annual cycle. (Curry et. al. 1995.) Melt ponds, on the other hand, are present in summer only. Thus an ideal study on melt pond coverage would span the whole melt season.

In this Master's thesis I will present a study on melt pond coverage near the drifting polar schooner *Tara* during a period of 28 days: 24. June to 21. July 2007. I have started out with a set of digital photographs obtained from a camera and computer unit mounted in *Tara*'s mast. By applying iterative image classification methods I have been able to partition the images into melt ponds and other surface types. I have calculated the percentage of melt ponds for 22 days out of 28. Six images have been left out of the analysis due to bad weather conditions causing poor visibility in the images. Using the results obtained for 22 days, I am able to present a time series on the evolution of melt pond coverage in an area of 6400 $m^2$ near *Tara* during 24. June to 21. July.

Unfortunately this time span does not cover the whole of melt season 2007. On July 21. the melt pond coverage is found to be approximately 15%, and there is cause to

suspect that the melt season is far from being over. It is a pity that there is but scarce data of melt pond evolution near *Tara* after 21. July. However, in several previous studies the melt pond coverage is obtained for one day only, or a few days at the most. I have been lucky enough to obtain a data set covering three whole months, out of which one month actually coincides with the melt period. Without the DAMOCLES campaign at *Tara* and the Karhukamera project, even this data set would not have been available.

I will start my work by discussing the basic optical and thermodynamical properties of sea ice. After dwelling on the basic physical relations in chapter 2, I will present a more qualitative description on melt season processes in chapter 3. In chapter 4 I introduce the instrumentation and measurement campaign that have enabled the collection of the data. I also make some general remarks on time lapse photography in geophysical research. In chapter 5 I discuss the methods I have chosen for data processing, and in chapter 6 I present my results. Chapter 7 concludes my thesis with a discussion on the results and suggestions for future campaigns.

# 2. Optical and thermodynamical properties of sea ice

## *2.1. Sea ice albedo*

Sea ice albedo is defined as the spectral irradiance directed upwards from an ice surface, as compared with the spectral irradiance incident on the same surface. Spectral radiance, denoted by $I(\theta, \phi, \lambda)$ is the power per unit area of ray of light in a particular direction, with a unit of W $m^{-2}$ $sr^{-1}$ $nm^{-1}$. When spectral radiance is integrated over the upper hemisphere as seen from a surface – in this case, the ice surface – the upwelling irradiance $F_u(0, \lambda)$ from that surface is obtained:

$$\int_{\phi=0}^{2\pi} \int_{\theta=0}^{\pi/2} I(\theta, \phi, \lambda) \cos(\theta) \sin(\theta) \, d\theta \, d\phi = F_u(0, \lambda) \qquad \textbf{(1)}$$

In the same manner, downwelling irradiance is obtained by integrating the radiance coming from the upper hemisphere as seen from the ice (that is, the sky):

$$\int_{\phi=0}^{2\pi} \int_{\theta=\pi/2}^{\pi} I(\theta, \phi, \lambda) \cos(\theta) \sin(\theta) \, d\theta \, d\phi = F_d(0, \lambda) \qquad \textbf{(2)}$$

In both cases, 0 denotes the ice surface, where $\theta=0$ and $\phi=0$. (E.g. Perovich 1998, 197.)

The amount of reflected solar irradiance depends on the wavelength of the incident radiation. The ratio of $F_u$ and $F_d$ is therefore called spectral albedo:

$$\alpha(\lambda) = \frac{F_u(0, \lambda)}{F_d(0, \lambda)} \qquad \textbf{(3)}$$

The fact that sea ice albedo is dependent on the wavelenght of the incoming radiation is a useful one for the study of melt ponds. (I will take a closer look at this in chapter 5.2.) However, the quantity that is often used instead of the spectral albedo is the total or bulk albedo, the integral of spectral albedo over wavelength:

$$\alpha_t = \frac{\int \alpha(\lambda) F_u(0,\lambda)\, d\lambda}{\int F_d(0,\lambda)\, d\lambda} \qquad \textbf{(4)}$$

The relevant wavelength range for the integration is that of optical radiation. Optical radiation refers to the portion of the electromagnetic spectrum where the sun emits most of its radiation, roughtly from 250 to 2500 nm. This region is divided into visible light (400–750 nm), ultraviolet light (250–400 nm) and near-infrared radiation (750–2500 nm). (Perovich 1998, 196.)

Figure 1 shows the theoretical spectral irradiance curve for a black body at the same temperature as the sun (5900 K), solar irradiance outside the atmosphere, and solar irradiance at sea level. The atmospheric gases responsible for the absorption are also indicated.

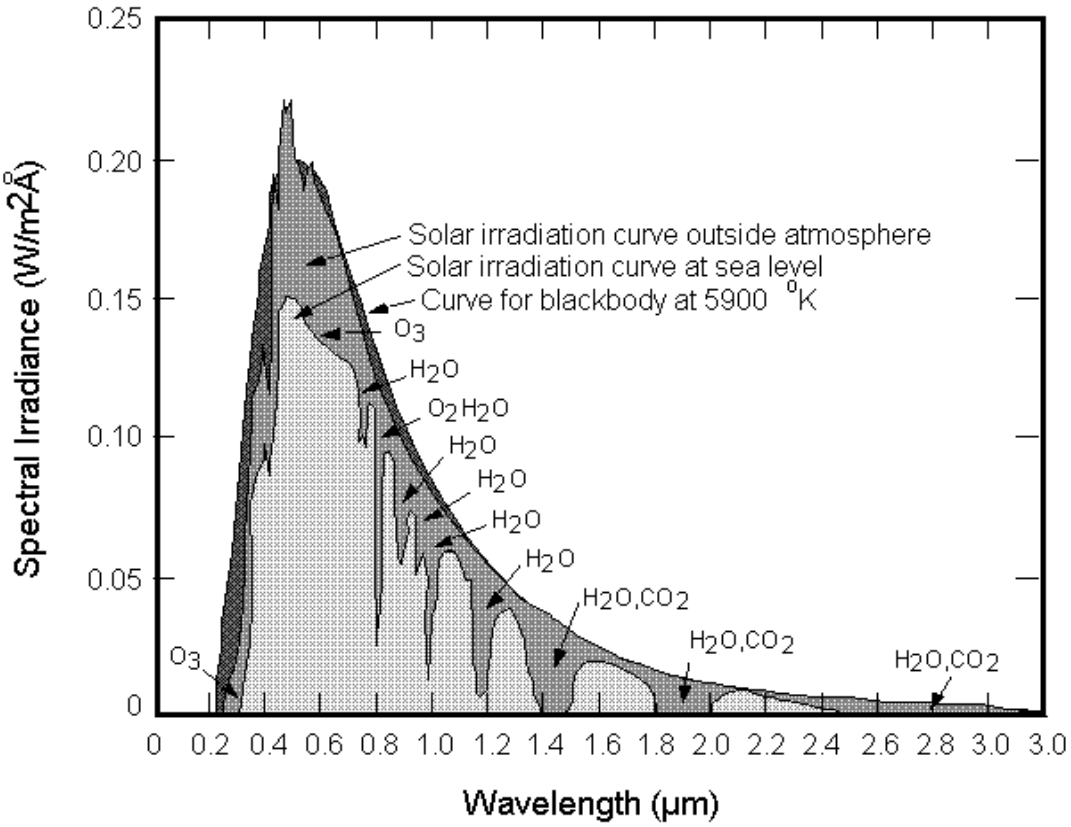


**Figure 1**: *Solar irradiance outside atmosphere and at the sea level. (Picture: The University of Texas at Austin, http://www.csr.utexas.edu/projects/rs/hrs/process.html)*

All the radiative energy at the surface of the earth does not originate from the sun. The earth itself, as well as its atmosphere, radiate in the infrared region. The maximum of earth's radiation lies at the wavelength of 12 µm, whereas the maximum of solar radiation is approximately at 0,5 µm. The two radiation bands do not overlap much, and therefore we can speak of short-wave radiation and long-wave radiation, where short-wave radiation is the same as optical radiation mentioned above. (E.g. Maykut 1986.) It is necessary to take both short-wave radiation and long-wave radiation into account, when looking at sea ice thermodynamics, for example. However, albedo is a quantity defined for short-wave radiation only. When speaking of albedo, I will always refer to the portion of optical, or short-wave, radiation reflected from the ice.

Typical values for some water, snow and ice surface albedos are shown in Figure 2. Open water has a low albedo, in the vicinity of 0,05, whereas new snow can have an albedo of nearly 0,90.

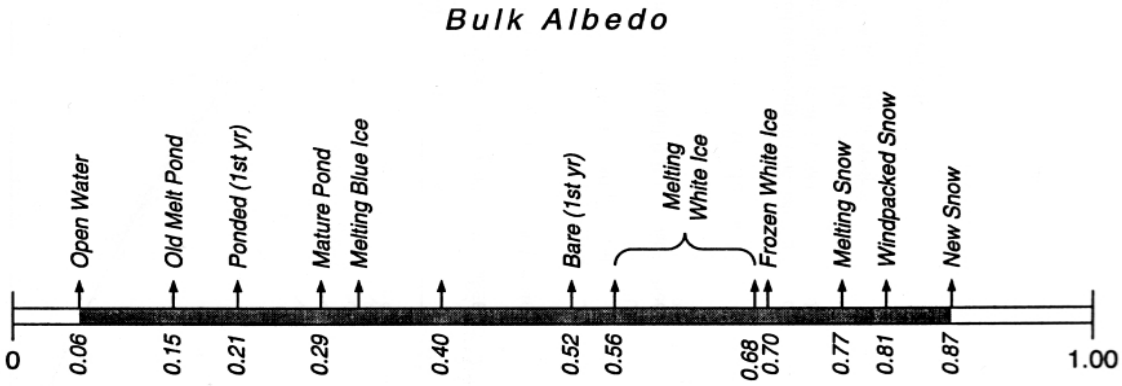


**Figure 2:** *Typical albedos for some sea ice surface types. Taken from Perovich (1998, 199). The data are from various sources: see Perovich (1998) for more information.*

Total albedo of a given surface is a function of both the surface spectral albedo and the distribution of the incident irradiance on that surface. Therefore changes in incident irradiance will modify the total albedo as well. An example of such modifying factor is cloudiness: on cloudy days the measured total albedo is greater than the total albedo measured under clear skies. Spectral albedos of various sea ice surfaces are often greater in the visible region than in the infrared end of the optical spectrum. Clouds, on the other hand, are efficient absorbers of infrared radiation. During cloudy weather conditions, a larger portion of the radiation reaching earth's surface will lie in the visible region, where albedo is also bigger. Thefore albedos measured in cloudy conditions are typically some 10% greater than albedos measured on clear and sunny days. (Perovich 1998, 210.)

All in all, albedo is the most studied optical property of sea ice. Total albedo is the measure of the solar energy absorbed by the ice and the ocean, and as such, it is a quantity of enormous importance. (Perovich 1998, 197.) To adequately understand and

model sea ice thermodynamics, especially in the context of the ongoing climate change, a lot of quantitative data and theoretical understanding of sea ice surface albedos is needed (e.g. Curry et. al. 1995; Curry et. al. 2001).

When solar radiation impinges on sea ice, reflection from the ice is just one possible mode of interaction. The portion of irradiance not immediately reflected from the ice surface is absorbed in the ice. Inside the ice, the electromagnetic radiation may scatter from the scatterers (mainly air bubbles) embedded in the ice, be absorbed in the ice, or be transmitted through the ice into the ocean below. (Perovich 1998, 200–206.) I will give a brief summary of these modes of interaction in the next chapter.

## 2.2. Basic sea ice thermodynamics

For sea ice surface to be in thermal equilibrium with the atmosphere, the conservation of energy requires the sum of all heat fluxes to the ice surface and away from it to be zero. This can be expressed as:

$$(1-\alpha)F_r - I_0 + F_L\downarrow - F_L\uparrow + F_s + F_l + F_c - F_m = 0 \qquad \textbf{(5)}$$

where:

$\alpha$ is the surface albedo

$F_r$ is the incoming short-wave flux

$I_0$ is the portion of short-wave flux penetrating through the surface into the body of ice

$F_L\downarrow$ is the incoming long-wave flux

$F_L\uparrow$ is the outgoing long-wave flux

$F_s$ is the sensible heat flux to the adjacent air

$F_l$ is the latent heat flux to the adjacent air

$F_c$ is the heat flux conducted to the ice

$F_m$ is the heat flux caused by melting at the surface

Although in this treatment I mainly refer to sea ice, equation 5 will also hold for a surface of snow on top of sea ice, with a pertinent choice of parameters (albedo, for instance, is different for snow and ice). (Wadhams 2000, 94–95; Thomas & Dieckmann 2003, 28–29.)

Sensible heat flux $F_s$ is the heat transferred by conduction from the ice surface to the air above, whereas latent heat flux $F_l$ is the heat released to the air by the surface snow or ice sublimating to a water vapour. The outgoing long-wave flux $F_L\uparrow$ is familiarly expressed as $F_L\uparrow \cong \varepsilon\sigma\ T^4$, where $\varepsilon$ is the emissivity of the surface, $\sigma$ is the Stefan-Boltzmann constant and T is the surface temperature. By definition, $F_L\uparrow$ and $I_0$ are directed away from the ice surface, which is indicated by the negative sign. $F_r$ and $F_L\downarrow$ are always directed towards the ice surface, so their sign must always be positive. $F_s$, $F_l$ and $F_c$ may be positive or negative, depending on the relative temperatures of the ice surface and the atmosphere. (Wadhams 2000, 94–95; Thomas & Dieckmann 2003, 28–29.)

The heat conducted to or away from the surface can be expressed as:

$$F_c = k_s \left(\frac{\partial T}{\partial z}\right)_0 \qquad \textbf{(6)}$$

where $k_s$ is the thermal conductivity of the ice and $(\partial T/\partial z)_0$ is the temperature gradient through the ice as measured at the surface, where z=0. When the surface temperature

$T_0$ is below freezing, there is no melting at the surface, and equation 5 can be written as:

$$(1-\alpha)F_r - I_0 + F_L\downarrow - F_L\uparrow + F_s + F_l = -k_s(\frac{\partial T}{\partial z}_0) \quad \textbf{(7)}$$

If, however, the surface is at the melting point and the overall heat flux to the surface is positive, the surface will melt. The heat flux related to the melting can be expressed as:

$$F_m = -L_i\rho_i(\frac{dh}{dt}) \quad \textbf{(8)}$$

where $L_i$ and $\rho_i$ are the specific heat and density of the ice, and h is the ice thickness. In the case of surface melting, equation 5 becomes:

$$(1-\alpha)F_r - I_0 + F_L\downarrow - F_L\uparrow + F_s + F_l + F_c = -L_i\rho_i(\frac{dh}{dt}) \quad \textbf{(9)}$$

(Wadhams 2000, 94–95; Thomas & Dieckmann 2003, 28–29.)

The study at hand focuses on the melting processes of both ice and snow on the surface of the ice. To understand the nature of melt ponds, however, it is important to understand the melt processes at the bottom of the ice as well. In order to grasp the situation at the bottom of the ice, it is necessary to look at the transfer of electromagnetic radiation through the ice.

Part of the incoming electromagnetic radiation is reflected at the surface, the percentage of the reflected amount being called the albedo. The rest of the radiation penetrates through the surface to the body of the ice. There it may be absorbed, perhaps after being scattered by air bubbles or brine pockets once or several times. And, finally, part of the short-wave radiation penetrates through the whole body of ice and is absorbed in the water below. (Wadhams 2000, 86–88.)

Electromagnetic radiation travelling in the ice obeys the extinction law of the familiar form:

$$I(z,\lambda)=I_0(\lambda)\exp[-\int_0^z \kappa(z,\lambda)\,dz] \qquad \textbf{(10)}$$

where $\kappa(z,\lambda)$ is the spectral extinction coefficient and z is the thickness of the ice travelled by the radiation. If $\kappa$ does not vary inside the ice, equation 10 can be simplified to:

$$I(z,\lambda)=I_0\exp[-\kappa(\lambda)z] \qquad \textbf{(11)}$$

The extinction coefficient is much larger for long-wave radiation, meaning that sea ice is highly opaque for the long-wave range of the electromagnetic radiation. Practically all of it is absorbed near the surface, and therefore its contribution can be ignored at the bottom. This means that if we want to write an equation akin to equation 5 for the bottom of the ice, terms $F_L\downarrow$ and $F_L\uparrow$ can be ignored. (Maykut 1986, 408; Wadhams 2000, 86–88.)

The electromagnetic radiation reaching the bottom of the ice is necessarily short-wave radiation Spectral extinction coefficient does depend on the wavelength even for short-wave radiation, but for the sake of simplicity a quantity called bulk extinction coefficient is defined, and noted as $\kappa_z$. It is obtained by weighing the contributions of different wavelengths for the short-wave radiation that has travelled through ice at thickness z:

$$\kappa_z = \frac{\int_0^z \kappa(\lambda) I(0,\lambda) d\lambda}{\int_0^z I(0,\lambda) d\lambda} \quad \textbf{(12)}$$

(Wadhams 2000, 86–88.)

According to this notation, the short-wave radiation reaching the bottom of the ice at thickness h can be written as:

$$I(h) = I_0 \exp(-\kappa_h h) \quad \textbf{(13)}$$

If the heat flux conducted through the ice and the heat flux from the water below do not balance at ice bottom, either melting of freezing will result. This may be written down as:

$$F_c + F_w + I(h) - F_m = 0 \quad \textbf{(14)}$$

where $F_w$ is the heat flux coming from the water.

It was noted before that a portion of the incoming short-wave radiation passes through the whole body of ice and is absorbed in the water. This term is not explicitly written in equation 14. However, the portion of short-wave radiation absorbed in the water increases the heat flux from the water to the bottom of the ice. This radiative contribution is therefore implicitly included in the term $F_w$.

Equation 14 presents the fluxes to and from the bottom of the ice. A more comprehensive approach is to think in terms of the temperature profile of the ice that generates those fluxes (or, seen the other way around, results from them). According to the heat conduction law, heat balance at the ice bottom can be expressed as:

$$k_i \frac{\partial T}{\partial z} - F_w = L_i \rho_i \frac{\partial h}{\partial t} \quad \textbf{(15)}$$

where $k_i$ is the thermal conductivity, $\rho_i$ is the density and $L_i$ is the specific heat of the ice. The shape of the temperature profile of the ice is the result of both conduction of heat and transfer of electromagnetic radiation in the ice. (Myrberg et. al. 2006.)

Thinking in these terms, the growth and decay of the ice, both at the surface and at the bottom, is all governed by the heat conduction law. The general formulation of the law is:

$$\frac{\partial}{\partial t}(\rho_i c_i T) = \frac{\partial}{\partial z}(k_i \frac{\partial T}{\partial z}) + q(z) \quad \textbf{(16)}$$

where q(z) is a heat source or sink inside the medium in question, in this case the ice. Claiming that there are heat sources or sinks in the ice is equivalent to saying the ice has a certain temperature profile, which results from the several heat fluxes to and

from the ice, and in turn contributes to maintaining those fluxes. (Myrberg et. al. 2006.)

At the surface, the heat conduction law can be formulated to give:

$$F_{tot} + k_i(\frac{\partial T}{\partial z}) = 0 \quad \textbf{(17)}$$

when the surface temperature of the ice is below the melting point, and

$$F_{tot} + k_i \frac{\partial T}{\partial z} = -L_i \rho_i \frac{\partial h}{\partial t} \quad \textbf{(18)}$$

when the surface temperature is at the melting point. (Myrberg et. al. 2006.) In this case, the sum of all fluxes except for the heat conducted to the ice is given as $F_{tot}$. This is, of course, what has already been stated in equation 5. In terms of fluxes, equation 17 is comparable with equation 5, and equation 18 with equation 7.

The treatment above could be made more thorough – and rather more complicated – by introducing discontinuities inside the ice, or by looking closer at the ice-snow surface below the blanket of snow. However, it is not within the scope of this work to give a deeper understanding of sea ice thermodynamics. Instead, in the next chapter I will give a more qualitative description of the melt season processes and melt pond formation.

# 3. Melt season and melt ponds

## *3.1. Melt season processes*

The snow cover on top of the Arctic sea ice typically starts to melt in June and is already gone by mid-July. As the snow melts, meltwater gathers in melt ponds. On first year ice these melt ponds start as shallow meltwater pools situated almost randomly on the ice surface. Naturally water tends not to gather on ridges or hummocks, but will flow into depressions on the ice. (Wadhams 2000, 56.) As more snow and ice melt and more melt ponds form, channels open up in between individual melt ponds, creating a network of pools and channels (e.g. Tschudi et. al. 2001; Perovich et. al. 2002; Grenfell & Perovich 2004).

As the melt season progresses, the melt pond fixtures become more permanent. Because melt ponds have albedos significantly smaller than the albedos of snow or bare ice, the ponds absorb more solar radiation than the surrounding icy or snowy areas, and start to deepen. As the ponds deepen, their diameter may diminish, so that the maximum melt pond coverage might actually be reached rather early in the melting season. (e.g. Fetterer & Untersteiner 1998.) If the ice survives its first melt season, the melt ponds that have not drained into the sea will again freeze in autumn. The sites of the refrozen melt pools will often show as depressions on the ice. As a result, multi-year ice is more undulating than a first-year ice sheet. (Wadhams 2002, 56–60.)

Wadhams remarks that every new melt season on multi-year ice deepens the old pond sites, since the melt ponds of the previous summer are the preferred locations into which the new meltwater starts collecting (Wadhams 2000, 60). Fetterer and Untersteiner (1998), however, present another view. They observe that mature ponds

often trap a lot of drifting snow in the autumn. As they fill with snow, capillary action elevates the water level, which subsequently elevates the level of the frozen pond site. According to Fetterer and Untersteiner, this process makes it unlikely that the old pond site will again become ponded in the following melt season. It is interesting that such contradictory views are presented, and it shows that even the basic characteristics of melt pool formation are not always agreed upon.

Because the melt pond site absorbs more radiation than its surroundings, ice will also start to thin at the bottom of the ice sheet, below the pond. Eventually the pond may eat its way through the ice, opening a thaw hole on the surface. If a thaw hole opens up, the water from the melt pond will be drained below the ice, where it may gather in an underside depression and form an under-ice meltwater pool. (Wadhams 2000, 56–57.)

Late in the melt season, the increased brine volumes inside the ice make the whole ice cover permeable to water. At this point, water can simply seep through the ice. This mode of drainage is mainly responsible for the pond area reduction in the late summer. In case of a thin ice cover, deepening melt ponds and meltwater drainage eventually lead into the ice melting completely and exposing ocean surface. (E.g. Fetterer & Untersteiner 1998.)

Those melt ponds not drained typically start to freeze again sometime in August. There may of course be cold spells during the Arctic summer, and some thin ice can form on top of melt ponds whenever the temperature drops below the freezing point. By the end of September all the ponds are likely to be frozen. (E.g. Perovich et. al. 2002a; Perovich et. al. 2002b.) I will discuss the melt pond coverage and some of its previous measurements in chapter 3.3. Before that, in chapter 3.2, I will give a short summary on melt pond albedos.

## 3.2. Melt pond albedos

Albedos of different surface types were already briefly listed in chapter 2.1. As a general rule, melt ponds have albedos from 0,2 to 0,4. The values are quoted from Perovich et. al. (1998); different researchers have measured slightly different values, depending on the observation site in question. However, it may be safely said that there is enough quantitative data on melt pond albedos to make good generalizations. Albedos have been measured for various types of ponds: young and old, deep and shallow, clean and dirty, etc.

Although all melt pond albedos are smaller than albedos of snow and ice, there is still considerable variation in between individual ponds. The range of melt pond spectral albedos is evident from visual observations alone: to the human eye, ponds may seem dark blue, light blue, greenish or nearly white[1]. This is a result of different pond types having a different spectral albedo: a pond that appears bluish, for example, has the highest albedo in the blue region. Or, to quote Donald K. Perovich: "[A]t least from 400 nm to 750 nm, what you see is what you get." However, it is not only the spectral signature that differs from pond to pond. The total albedos between different types of ponds may also vary as much as by a factor of 2. (Perovich et. al. 1998.)

Spectral albedos for several melt pond types have been plotted in Figure 3, along with albedos for wet and dry snow.

1 Deep ponds appear blue, ponds with algae or other organic material present appear green, and shallow pools with bubbly ice beneath the water appear white. (E.g. Eicken et. al. 1994; Tucker et. al. 1999.)

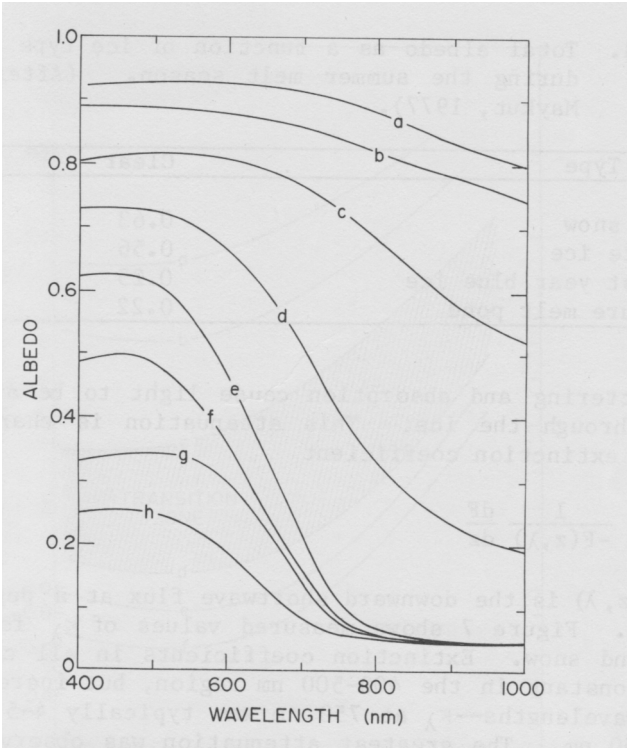


**Figure 3**: *Spectral albedos for dry snow (a), wet new snow (b), melting old snow (c), partially refrozen melt pond (d), early season melt pond with white bottom on multi-year ice (e), mature melt pond with blue bottom on multi-year ice (f), shallow melt pond on first-year ice (g) and old melt pond on multi-year ice (h). (Grenfell & Maykut 1977; Untersteiner 1986.)*

Although the albedos for different snow, ice and pond types can be measured, the question: "What is the total albedo of sea ice?" is still not easy to answer. During the melt season, the snow cover on top of the ice as well as the ice surface itself undergo significant transformations. The ice starts to display a marked horizontal variability in its surface conditions. There may be snow-covered ice, bare ice, melt ponds and open leads, all present in roughly the same area at the same time. (E.g. Derksen et. al. 1997; Perovich et. al. 1997; Perovich et. al. 1998.) An example of such surface patchiness is presented in Figure 4.

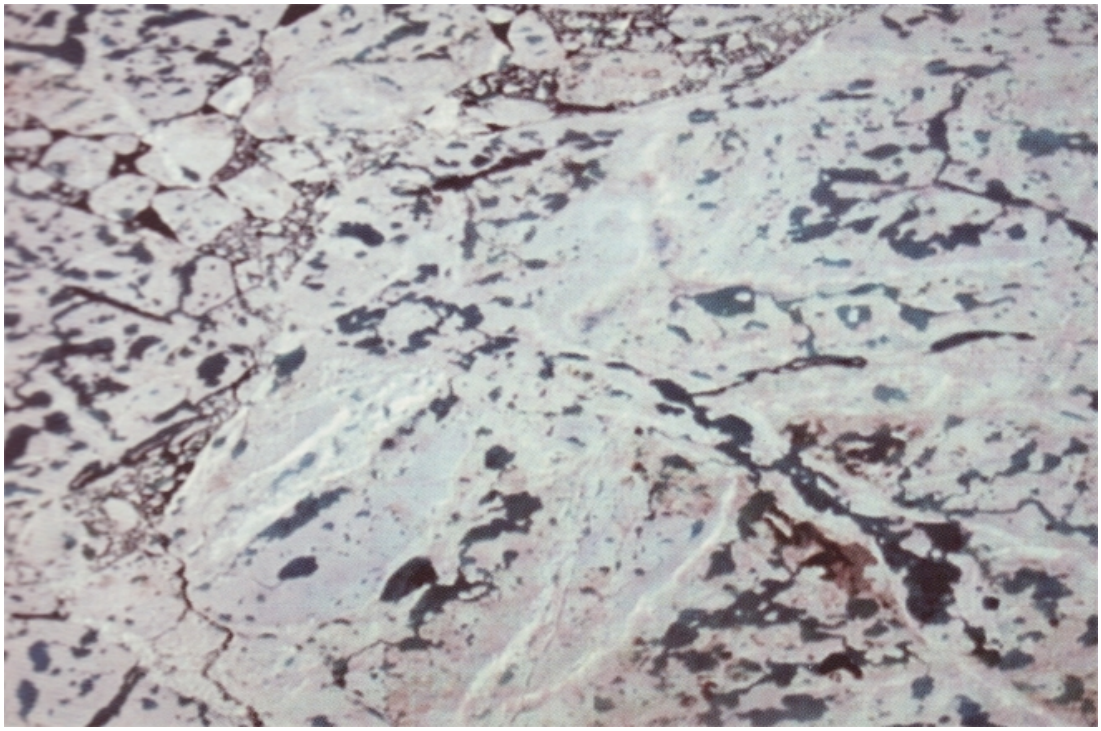

**Figure 4:** *Snow, bare ice, melt ponds and leads; an aerial view. (Photograph: Thomas & Dieckmann 2003)*

If the fractional areas covered by ice (bare or snow-covered), melt ponds and open water are expressed as $A_i$, $A_p$ and $A_w$, respectively, and if and the albedos of those areas are $\alpha_i$, $\alpha_p$ and $\alpha_w$, the regional albedo can be expressed as:

$$\tilde{\alpha} = \alpha_i A_i + \alpha_p A_p + \alpha_w A_w \qquad \textbf{(19)}$$

where:

$$A_i + A_p + A_w = 1 \qquad \textbf{(20)}$$

(Fetterer & Untersteiner 1998).

A more sophisticated model may take into account a greater number of distinct surface types, but the same basic relation should hold:

$$\tilde{\alpha} = \sum A_j \alpha_j \quad \textbf{(21)}$$

(Tschudi et. al. 2001).

Because melt ponds and leads have a lower albedo than ice and snow, the melting processes lead to an overall diminution of the total regional albedo. Based on the results of the SHEBA campaign (Surface Heat Budget of the Arctic), Perovich and Tucker (2002b) have estimated that the total albedo of sea ice drops from 0,8–0,9 in April to 0,4 in August. The first diminution happens already in April–May, when the snow on top of the ice gets warmer and its grain size increases, leading to more absorption. When actual melt ponds start forming, there is a sudden decrease in albedo, from 0,7 to 0,5. This rapid change may take place in just one week's time. As the melt season progressed and melt ponds matured, Perovich and Tucker measured even further reduction in albedo, down to 0,4 in August. (Perovich & Tucker, 2002b.)

It is clear that melt ponds play a significant role in sea ice thermodynamics during the melt season. When the sea ice albedo diminishes in summer, more radiation is absorbed in the ice; the increased absorption of radiation accelerates melting, which further decreases the albedo. This is known as the sea ice-albedo feedback mechanism. Therefore an increase of the global temperature may diminish the total albedo of the sea ice, which will again accelerate the warming – or so it is believed. Melt ponds and their albedos are important factors to be taken into account here, since the melt pond fraction significantly affects the total sea ice albedo. In fact, sea ice albedo reaches its minimum when melt pond fraction is the highest. (E.g. Curry et. al. 1995; Curry et. al. 2001.)

## 3.3. Previous research on melt pond coverage

Measurements of melt pond coverage are almost invariably done on Arctic sea ice. Melt ponds do not feature largely on Antarctic sea ice, because the ice formed in the Antarctic is much less stable than in the Arctic: for the most part it moves northwards, spreads out, and disintegrates at the retreating edge. Melt pools do occur on Antarctic multi-year ice, but multi-year ice only forms in certain specific regions of the Antarctic (for example Weddell Sea, Ross Sea and Bellingshausen Sea). (Wadhams 2000, 57, 64.)

In the Arctic, however, summer time melt pools play a large role in determining both the small and large scale properties of the sea ice. To assess the significance of melt ponds in determining the total sea ice albedos, it is necessary to gather more information on the pond coverage, as well as the temporal duration of the ponds. One way of obtaining this information is acquiring photographs or summer sea ice and processing them in such ways that the areal melt pond coverage becomes known. This is precisely what I have set out to do in this study, and in this chapter I will take a look at some previous studies done in the same manner.

Fetterer and Untersteiner (1998) point out, that although pond albedos do vary, in the visible region (400–700 nm) there is still approximately a 30% difference in albedo between an early pond and snow or multi-year ice. In photographs of the ice surface, ponds look markedly different from melting snow or multi-year ice, even if, for example, melting snow and melting multi-year ice cannot be told apart. In many cases the distinct shape and clear edges of melt ponds enable the ponds to be recognized from photographic data. (Fetterer & Untersteiner 1998.)

Photographs, aerial or otherwise, are just one possible means of studying the melt pond coverage. The areal extent of melt ponds can also be assessed by direct measurements done on the ice, for example by setting up a survey line and measuring the extent of melt ponds along the line (e.g. Perovich et. al. 2002b). The advantage of photographic data is that it allows the melt pond coverage to be obtained from a significantly larger area than could be examined directly on the ice.

Pond coverages from various photographic data have been calculated by Hanson (1961), Langleben (1969, 1971), Eicken et. al. (1994), Derksen et. al. (1997), Tschudi et. al. (1997), Perovich & Tucker (1997), Fetterer & Untersteiner (1998), El Naggar et. al. (1998), Tucker et. al. (1999), Tschudi et. al. (2001) and Perovich et. al. (2002a). From the 1990's onwards, modern digital image processing techniques have been made use of to obtain the melt pond coverage from digitized photographs. The results obtained from the studies listed above are presented in Table 1.

Although the melt pond coverage has been studied to a reasonable extent, during more than four decades, it is clear that no simple generalizations can be made based on the available results. This is partly due to the fact that research campaigns up in the Arctic are hard and costly. It is not easy to obtain sea ice observations that both cover a large areal extent and span a reasonably long time frame.

Most campaigns presented in Table 1 cover a temporal range varying from one day to two weeks, which means that their results represent only a particular phase of the melting season. The greatest number of measurements have been done in Beaufort and Chukchi Seas, and the results cannot necessarily be generalized for the whole Arctic region. And even when the above limitations are taken into account, it is still not clear that a reliable synthesis can be made of the melt pond coverages presented in Table 1.

**Table 1**: *Melt pond coverages measured from photographs, 1962–2002.*

| Published by | Campaign | Location | Duration | Instrumentation | Obtained pond coverage |
|---|---|---|---|---|---|
| Hanson, Kirby J. 1961 | UNSHO 1949 (U.S. Navy Hydrographic Office) | Beaufort and Chukchi Sea | July and August 1948 | Airplane and camera (analogue) | 20% - 40 % |
| Langleben, M. P. 1969 | Ice Research Project, Department of Physics at McGill University | Tanquare Fiord, Ellesmere Island | 12. May – 17. June 1968 | Camera (analogue) mounted 6 m high in a tower | Maximum of 80% |
| Langleben, M. P. 1971 | Ice Research Project, Department of Physics at McGill University | Beaufort Sea, near Tuktoyaktuk | 16 days in June 1969 | Helicopter and camera (analogue) | Maximum of nearly 80% |
| Eicken, H. et. al. 1994 | ARCTIC 91<br>ARCTIC 93 | Eurasian Arctic | 2 days in August 1991<br>4 days in August 1993 | Helicopter and video camera (analogue) | Average of 16 % in 1991<br>Average of 19 % in 1993 |
| Derksen, C. et. al. 1997 | SIMMS (Sea Ice Monitoring and Modelling Site) | Canadian Arctic Archipelago (~74°N) | 7.-9. July 1995 | Balloon in 300 m and camera (analogue) | Maximum of 53 % |
| Perovich, Donald K. et. al. 1997 | Arctic Ocean Section cruise | 76°N 172°W | 31. July 1994 | Helicopter and camera (analogue) | Average of 12 % in 20,5 $km^2$ |
| Tschudi, Mark A. et. al. 1997 | BASE (Beaufort Arctic Storms Experiment) | Beaufort Sea (~72°N) | 21. September 1994 | Airplane and CCD video camera | Average of 20±8 % |
| El Naggar, S. et. al. 1998 | NEWP (Northeast Water Polynya) expedition | Northeast Water Polynya (~78°N) | 6.-30- July 1993 | Helicopter and line scan CCD camera | 34,2±14,26 % on first-year ice<br>19,0±6,85 % on multi-year ice |
| Fetterer, Florence & Norbert Untersteiner 1998 | Classified data from NTM (National Technical Means) systems | Beaufort Sea | July 1993<br>July & August 1994<br>Entire summer 1995 | Single channel, visible range satellite instrument | 40-50 % on first-year ice<br>30 % on multi-year ice |
| Fetterer, Florence & Norbert Untersteiner 1998 | AIDJEX (Arctic Ice Dynamics Joint Experiment) | 75°N 142°W | 12. July 1975<br>18. July 1975<br>3. August 1975 | Helicopter and hand held camera (analogue) | Same results as above (this was additional data in the same study) |
| Tucker, William B. et. al. 1999 | Arctic Ocean Section Cruise | Arctic Ocean (76°N-88°N) | 31. July 1994<br>13. August 1994<br>18. August 1994 | Helicopter and camera (analogue) | 12% at 76°N (31. July)<br>3% at 84°N (13. August)<br>Only frozen ponds at 88°N |
| Tschudi, Mark A. et. al. 2001 | SHEBA (Surface Heat Budget of the Arctic Ocean) | Beaufort and Eastern Chukchi Sea (~78°N) | 5 days in July 1998 | Airplane and CCD video camera | Smallest 24,6±6,2 % (8. July)<br>Largest 34,1±8,4 % (24. July) |
| Perovich, Donald K. et. al. 2002 | SHEBA (Surface Heat Budget of the Arctic Ocean) | Beaufort Sea | Twelve days in 5. April - 4. October 1998 | Helicopter and camera (analogue) | Maximum of 24 % (7. August) |

Although all studies listed in Table 1 set out to assess the areal coverage of melt ponds, in a specific region of the Arctic at a specific time, the quantities obtained are not always comparable. Some researchers have presented the maximum areal extent of the ponds as their main result, whereas some have calculated the average extent of the ponds during the period of data collection. When some kind of average has been obtained, it is not always clear, how large is the area studied. In some cases, the percentage of the ponds is calculated in relation to the *whole* area studied, open leads included, whereas in others, the pond percentage is the ratio of ponded ice in relation to all the ice but not the leads. Some researchers have made a distinction between first-year and multi-year ice, while some have not.

For the most part, melt pond fractions are determined with the aid of digital image processing techniques, and the resulting accuracy is not always easy to determine. In fact, most of the studies mentioned in Table 1 have not even attempted to quantify an estimate for the resulting error. Where a numerical error estimate has been given, the margin of error is assessed to be rather large: 40% in Tschudi et. al. (1997), 42% for first-year ice and 36% for multi-year ice in El Naggar et. al. (1998), and 25% for both first-year and multi-year ice in Tschudi et. al. (2001). The estimated errors have diminished, as the digital image processing techniques have become more advanced. However, there is still a demand for more accurate measurements and further studies in diverse regions of the Arctic, especially in the central Arctic Basin.

# 4. Instrumentation

## 4.1. Karhukamera project

Karhukamera is a camera system designed by a group of Finnish individuals, loosely connected with the Astronomical Association of Pori (”Porin Karhunvartijat”). The group has developed various camera units, which can be used for compiling time lapse photography data sets. The project is named Karhukamera.com, and has its web page in that address (http://www.karhukamera.com). The first camera unit built by the project was designed to provide remote weather observations at the site of the astronomical observatory, but as the project has grown and matured, several camera units have been assembled and different set-ups are currently being tried out.

From the year 2006 there has been some collaboration with Karhukamera and Finnish Institute of Marine Research (FIMR). The collaboration has been facilitated by Jari Haapala at FIMR and Eero Rinne (currently at Edinburgh University, School of GeoSciences). A Karhukamera camera unit has been made use of during the DAMOCLES field campaign on board *Tara*, resulting in the photography data set being studied in the work at hand.

## 4.2. Data acquisition

It was suggested by a Norwegian scientist and explorer Fridtjof Nansen that a ship inserted into the pack ice off the coast of Siberia would drift across the Arctic Basin and end up in between Svalbard and Greenland. Nansen undertook to prove this theory

and made his historical voyage with the ship *Fram*, which indeed drifted across the Basin in a three years' time (1883–1886). (Weeks 1998, 8.)

More than a hundred years later, a French private schooner *Tara* (specifically built for the purpose) and her crew undertook to repeat the voyage of *Fram*. The expedition was led by Etienne Bourgois and sponsored by fashion company *agnés b*. (Gascard et. al. 2008.) *Tara* is shown in Figure 5, immersed in ice, with her hull almost buried in the snow.

**Figure 5:** *The polar schooner Tara immersed in pack ice. (Photograph: Marcel Nicolaus, Norwegian Polar Institute)*

*Tara* was anchored into the pack ice off the coast of Siberia, north of Laptev Sea, on 3. September 2006. She reached her northernmost point (88°32') on 28. May 2007. The French ship thus broke the record previously held by *Fram*, and is now the ship that has reached the northernmost point by drifting immersed in the Arctic pack ice. (*Tara* Expeditions home page, saved 31.3.2008.) *Tara* exited the ice at at the west side of the

Greenland sea on 21. January 2008. Because the ice drift across the Arctic basin is faster today that it was in Nansen's time, *Tara* drifted for 15 months to complete the journey that took Nansen three years. (Gascard et. al. 2008.)

In spring 2007 *Tara* hosted a research camp for European scientific programme DAMOCLES (Developing Arctic Modeling and Observing Capabilities for Long-term Environmental Studies). DAMOCLES is a joint European research effort designed for studying climate change in the Arctic. The programme is funded by the European Union and run by the DAMOCLES consortium, consisting of 48 scientific institutes in 11 European countries, the Russian Federation and Belarus. Finnish Institute for Marine Research is one of the facilities involved in the DAMOCLES consortium. (Gascard et. al. 2008.)

Fifteen scientists of seven nationalities took part in the DAMOCLES scientific camp on board (or, more accurately, in the vicinity of) *Tara* during April 2007, two of them (Jari Haapala and Eero Rinne) from Finnish Institute of Marine Research. Various measurements of the atmosphere, the sea ice and the ocean were performed on the drifting station, in order to gain more understanding on processes determining the evolution of the pack ice, and to gather data for the development of numerical sea ice models and remote sensing retrieval algorithms. (Gascard et. al. 2008.)

One of the instruments the FIMR researchers brought along was a Karhukamera camera unit R!MU (“Really! Moving Unit”). The unit consisted of a camera, a computer and a GPS instrument (Holux GR-213 SiRF Star III), placed inside a protective casing. The unit is shown in Figure 5, complete but for the GPS instrument. Technical details of the camera are given in Table 2.

**Table 2:** *Technical details of the camera inside Karhukamera R!MU unit.*

| | |
|---|---|
| Manufacturer | Olympus Imaging Corp. |
| Model | SP 350 |
| Resolution | 2048x1536 |
| Focal length | 8 mm |
| Mode of exposure | automatic |
| Exposure time | 1/1600 s–1/10 s |
| Aperture | f/2.8–f/8 |
| ISO | 50–155 |

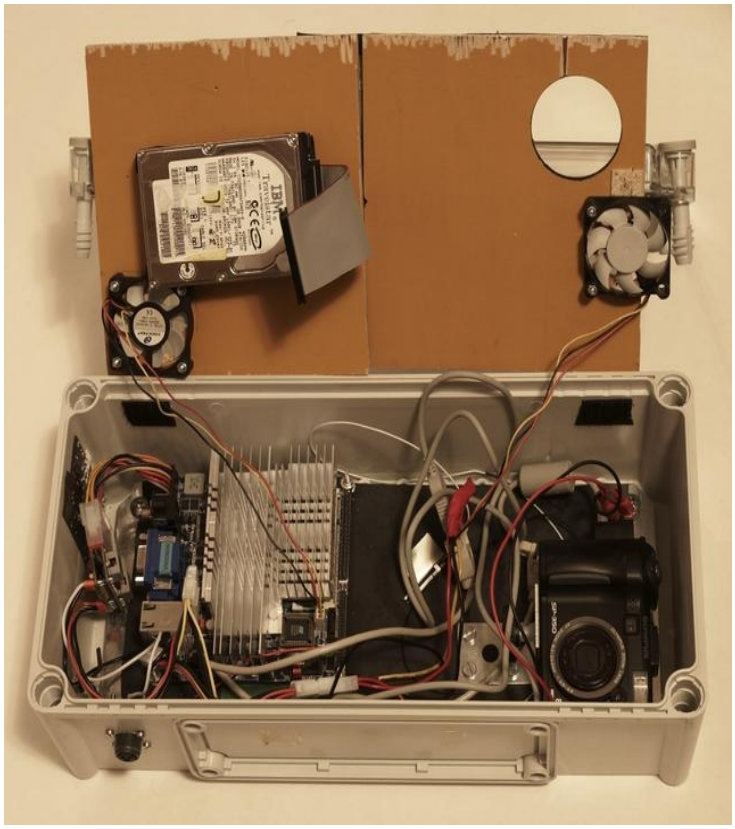

**Figure 6**: *Karhukamera R!MU unit (camera & computer) inside the protective casing. (Photograph: Mikko Viitapohja, Karhukamera)*

The Karhukamera unit, inside its casing, was mounted in the height of approximately 7 metres in the mast of *Tara*. The camera was operational from 29. April to 22. July, automatically obtaining photographs in a 10-minute interval. The photographs were stored in the 20 GB hard disc of the camera unit, until both camera and computer were returned to FIMR and the photographs could be retrieved. They were then uploaded

into a database along with their technical specifications, as well as GPS-data obtained from the GPS instrument included in the set-up. The resulting database contains a total of 12192 photographs. The area covered in this study is 6390m$^2$, with the resolution of the perspective-corrected photographs corresponding to 5 cm x 5 cm on the ice.

Photographs were obtained at a 10-minute interval during a period of almost three months, in which the melting season starts and gets well under way. The temporal variation of the individual ponds, as well as the total pond coverage, is therefore of interest. For unknown reasons, the camera unit stopped functioning already on 22. July. However, three months is already a rather lengthy data collection time in these matters, especially as the measurements were done up in high Arctic, on the drifting pack ice itself.

*Tara*'s track during the data collection period is shown in Figure 7. 29. April is the day of installation, and the main results presented in this thesis cover the time span from 24. June to 21. July.

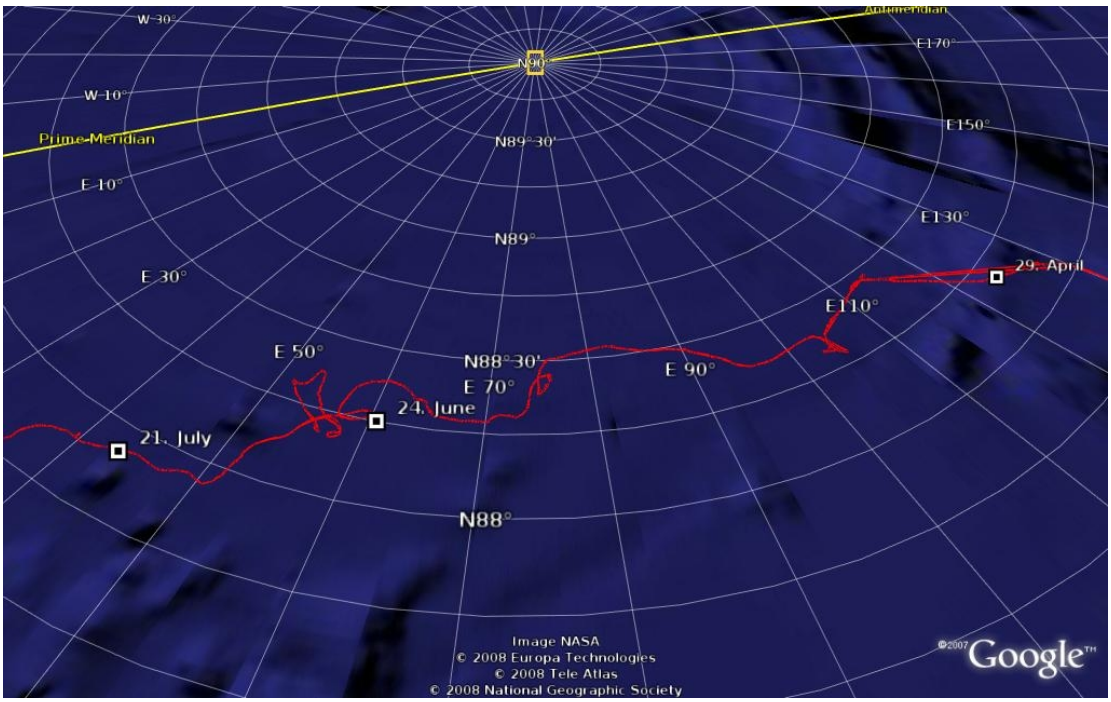


**Figure 7**: Tara*'s track from 29. April to 21. July. Courtery of Tara Expeditions.*

## 4.3. Time lapse photography as a tool for research

Time lapse photography is a tool well suited for many types of geophysical research, and for sea ice research in particular. Sea ice undergoes both slow and rapid changes, and with a suitable interval in between the individual photographs, it is possible to monitor both long-term and short-term evolution of ice. In this chapter I will give some examples of time lapse photography being used as a tool for research.

Finnish Institute of Marine Research has continued their collaboration with Karhukamera project after the Tara campaign. Another Karhukamera camera unit was mounted on board a Norwegian research vessel R/V Lance for a 15-day campaign in September 2007. The purpose of the set-up was to find out whether such a camera unit will function reliably, even when mounted on board a ship travelling in heavy ice conditions.

The results of the *R/V Lance* campaign were highly promising; the camera unit did work throughout the test period, and even the test data obtained during the cruise may yet prove useful. (I will present an example of the data obtained from *R/V Lance* at the end of chapter 7.) As a result of the initial co-operation, FIMR has now purchased one Karhukamera unit for their future use.

The Finnish Meteorology Institute (FMI) has also started co-operating with Karhukamera during spring 2008. They have arranged a Karhukamera unit to be mounted on a helicopter during a SNORTEX (SNOw Reflectance Transition EXperiment) campaign in Sodankylä, Northern Finland. The purpose of the set-up is to obtain leaf area indexes from the terrain below. (Eero Rinne, personal communication, 3.4.2008.)

Finnish Institute of Marine Research has also made use of another automatic camera system, IceCam, during a winter campaign in 2006. In her Master's thesis, Hanna Leisti (2007) examines sea ice compression events in the Baltic Sea, using a data set obtained from a camera mounted on icebreaker *I/B Otso*. The camera in question is a 0,3 megapixel web camera, developed jointly by the Scottish Marine Institute (SAMS) and the Norwegian Polar Institute (NPI). The camera itself was borrowed from the Norwegian Polar Institute.

IceCam was on board *I/B Otso* from 2. February to 9. May 2006. It was mounted on the ship roof, facing backwards, and automatically obtained photographs from the ice field behind the ship. The interval between photographs was one minute. Nearly 138 000 images were saved during the period of data collection. In her study, Leisti selects five separate ice field compression events from the obtained data and calculates the magnitude of compression for those events. The obtained values are compared with theoretical models of sea ice motion and ship motion in compressive sea ice. (Leisti 2007.)

IceCam camera units similar to the one used in Leisti's study are also set up in Greenland. A total of 12 IceCams have been installed at six different glaciers in order to monitor Greenland glacier discharge variability. The study is supported by NASA and is a part of the International Polar Year 2007–2008 research. (Automatic Ice Cameras home page, saved 31.3.2008.)

The short list of campaigns presented here illustrates the ample possibilities of time lapse photography as a tool for research: a time lapse photography data set can be used to monitor melt pond coverage, ice field compression, glacier drainage and leaf coverage, just to name a few applications.

# 5. Methods

## 5.1. Image correction

Before the analysis could start, many different types of image corrections needed to be performed on the original data. Figure 7 is an example of the relatively unprocessed photographic data I started to work with. Of course, as a jpg-file, the picture has already been compressed somewhat, and is no longer the original data created by the camera itself. However, it is beyond the scope of this work to discuss the inner workings of a digital camera, or to go into any detail about different image formats and modes of compression. To the intents and purposes of this study, the jpg-compressed photograph files are as close to the original data as need be.

Figure 8 is taken towards the end of the data collection period, on 17. July 2007 at local noon. Melt ponds are clearly present on ice: they show up blue against the white snow. Besides the melt ponds, some other less wanted features are immediately visible. Since the camera is mounted in the mast of the ship, some of the riggings cut across its field of view. These present no serious problem later on, since they can be successfully classified as something spectrally very different from snow and melt ponds.

The crooked horizon is another unwanted effect; or, rather, a problem stems from the fact that the crookedness of the photos varies from time to time. Although the camera was mounted in a stable position against the mast, the angle of the photographs taken varies across the data set. That is due to the movements of the ship during the summer months. *Tara* was stuck inside the pack ice, but the ice itself underwent some deformations along the way. As a result, the ship shifted her position several times.

These events can be easily tracked, since it is possible to view the whole data set as a video. It is clear that the position of the ship is not constantly shifting, just at certain well-defined times. After locating the shifts, the images can be adjusted so that the horizon is no longer tilted.

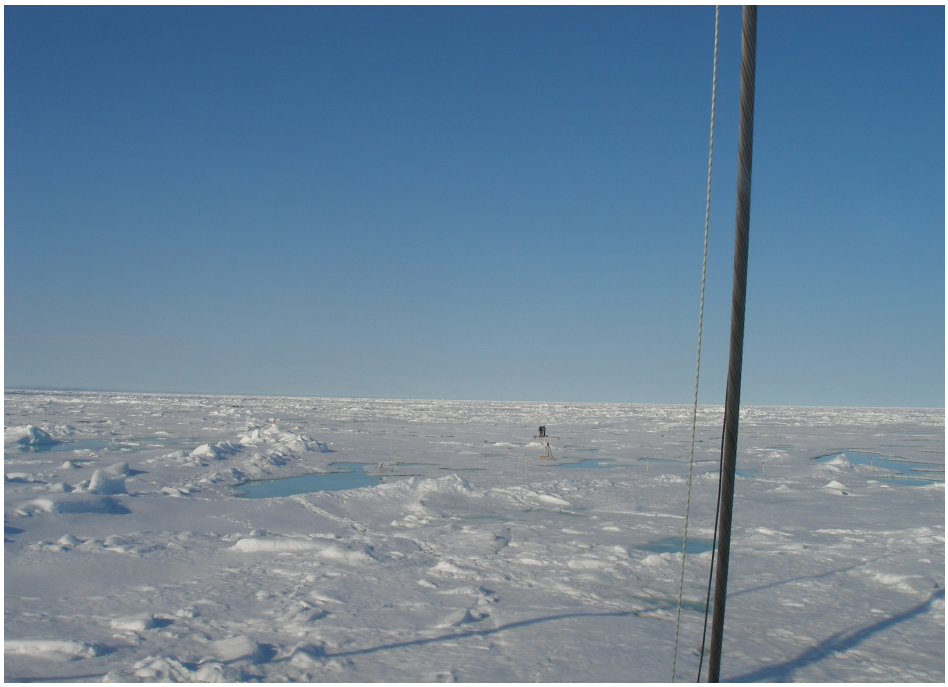

**Figure 8**: *A Karhukamera photograph of the ice, taken 17.7. 2007 at local noon.*

Because the aim of this study is to assess the temporal evolution of melt pond percentage in the area in question, it is necessary to be looking at the same area throughout the analysis. If the viewing angle of the camera varies due to the movements of the ship, the area chosen for the analysis from each picture doesn't necessarily correspond to the same physical region of the ice. This may or may not be a problem, according to the melt pond distribution and the dimensions of the area being analyzed. If the area were large enough, results would be representative for a bigger region than just the chosen area, and it wouldn't matter so much if the actual physical area being analyzed changed somewhat during the analysis. However, since the physical area looked at in this study is only some 71 m x 90 m, it is safest to

remove the crooked horizon effect, and to look at the evolution of the same area throughout the whole period of data collection.

Yet another effect to be removed is the barrel distortion. Barrel distortion means that the closer an area lies to the optical axis of the camera, the bigger it will appear in the final photo. The effect varies according to the type of lens being used: a wide lens angle will cause more barrel distortion than a narrow one. The way to remove this effect is to use a test image of a grid – a chess board, for example – taken with the same camera as the data under analysis. From the distorted image of the grid, the amount of distortion can be calculated, and thus the desired correction is obtained. In fact, any geometrical lens distortions are removed at the same go, whether they are caused by the barrel effect or something else – a defect in the lens, perhaps.

The barrel distortion correction to the Karhukamera data set was done by István Heiler from Finnish Institute of Marine Research. Figure 9 is the same photograph as in Figure 8, with the barrel distortion removed. In this case the barrel distortion has been quite small, since it is hard to perceive much difference in between the two images.

**Figure 9**: *The image from 17.7.2007, after barrel distortion correction.*

After taking care of the horizontal tilt and barrel distortion, one more important image processing procedure remains to be done: perspective correction. As stated above, barrel distortion arises from the specificities of the camera lens, and the crooked horizon problem is caused by the camera and the whole platform it resides upon – that is, the ship – moving about. Perspective distortion, on the other hand, is present in any photograph. A point in a photograph corresponds to a larger area in the real physical world, the further away the object or terrain being photographed actually lies. This is, of course, the way our own visual perception works as well: faraway objects seem smaller than those of similar size, but closer. This is unavoidable, and does cause problems, when different areas in the same photograph are to be compared with each other.

István Heiler, who performed the lens distortion correction for the data set, also created a program that removes the perspective distortion and allows the image to be

presented in an x,y -frame corresponding to the distances in the physical world. Matematically this is a fairly straightforward procedure, as long as the height of the camera is known. And therein lies another source of error: as the ship has been moving about in the ice, the height of the camera in relation to the ice has changed at times. To be able to reliably perform the perspective correction, one needs some sort of measure stick for calibration purposes.

In this case, such measure sticks abound in the photos. Several measuring campaigns have been carried on nearby *Tara* all through the melt season, and a snow depth measurement line cuts horizontally across the camera's field of view. The line consist of literal measuring sticks standing on the ice, separated from each other by some 10 metres. I've chosen one image for the calibration purposes (the noon image from 29. June 2007) and chosen the camera height to be 5,308 m: in this way, the distance spun by four snow measurement poles corresponds to exactly 40,00 m in the perspective corrected image.

In reality the poles might not be exactly 10 m apart. The accuracy of value 40,00 m is chosen for the image correction purposes, not because it reflects the exactness of pole placing on the ice. According to Jari Haapala and Eero Rinne, the error made in pole placement might be as much as 1 metre (that is, 10%). However, if all perspective corrected images maintain the same length scale, the pond areas in different images should be comparable with each other. After all, the pond coverage is to be obtained as a percentage, not as an absolute value.

In practice, the perspective correction procedure is made in two steps. After an image is deemed suitable for analysis – I will specify the criteria for suitability later on – the placements of the snow measurement poles are determined from the original image. In theory, only two points are needed: for example, the lower ends of the two outmost

poles, in the row of poles that – also in the realm of theory – is exactly 40,00 metres long. In practice, the two poles furthest away from each other might not be ideal for the calibration of every single image in the data set. Even at the height of the Arctic midsummer it frequently snows, and snow may easily pile up at the foot of any given pole. This presents a problem, because the perspective correction needs to be calibrated with points that have zero elevation from the surface of the ice.

Luckily, even after snowfall, all the poles are not equally immersed in snow. In almost every image it is possible to discover at least two poles not too deep in snow, and to use the distance between the lower end of those two poles for the calibration purposes. The calibration distances of all the poles are similarly obtained from the test image.

When the suitable calibration points are chosen from the image that is to be corrected, a test run is made with an initial guess for the height of the camera. A programme designed by István Heiler calculates the distances of the poles after the transformation, and if the result is the same as it was for the test image, the height of the camera has been correctly guessed. Since the ship only moves a few times per month, it is usually a good policy to estimate that the height of the camera has not changed in between two consecutive images. If, however, the ship has shifted her position, the height of the camera will have changed, and the incorrect height parameter needs to be adjusted.

The adjusting of camera height goes on, until the chosen distance parameter lies within 1 cm of its test image counterpart. After that, it is concluded that the camera height is known with a reasonable accuracy, and the perspective correction can be performed. Figure 10 shows the same photograph as in Figure 8 and Figure 9, after the perspective distortion has been removed. The upper portion of the image, the sky, has also been cut off, because it is not needed in the further analysis of the image.

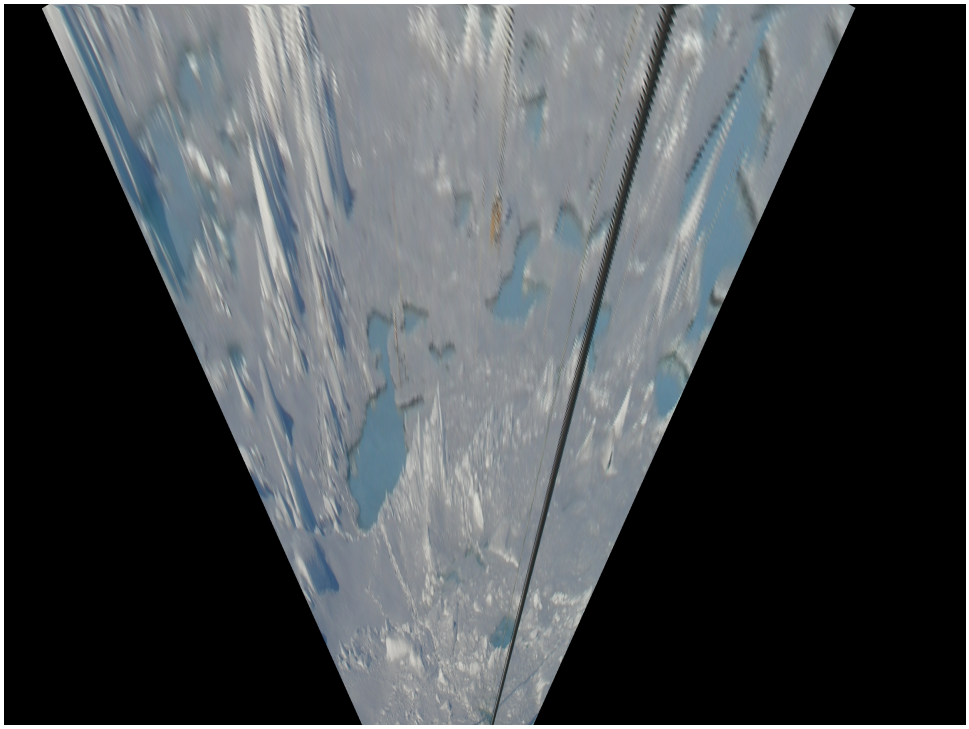

**Figure 10**: *The image from 17.7.2007 after the perspective correction.*

## 5.2. Alternative image partitioning methods

After the images have been corrected in ways described in chapter 5.1, all the pixels in the new images correlate with a 5 cm x 5 cm region of the ice. Now the pixels can be compared with each other, and if the number of pixels that coincide with ponds is known, the pond coverage is easily obtained. The question that remains is: how to distinguish the pond pixels from all the other pixels? There are several digital image analyzing techniques, widely used in field of remote sensing, that can be applied to this purpose.

Before the time of digital image processing, pond areas were simply measured from film photographs with a planimeter (Langleben 1969, 1971). In more modern studies, melt puddles have been distinguished from surrounding ice (and possibly also open water) in several different ways:

- When working with digital greytone images, by visually and manually defining a suitable greytone threshold to separate the pond pixels from brighter snow pixels (Eicken et. al. 1994; Derksen et. al. 1997; El Naggar et. al. 1998)
- By using the contrast between the blue and red bands: calculating the numerical values of blue band pixels minus red band pixels, thus getting a greytone image as a result, and then selecting a suitable greytone value to separate the ponds (Tschudi et. al. 1997 2001)
- By supervised classification with maximum likelihood algorithm and manually chosen training areas (Fetterer & Untersteiner 1998)

In some cases, the method of partitioning the image into pond and ice classes is not fully disclosed: images are said to be "processed [...] using standard commercial software" (Perovich & Tucker 1997), "processed using image analysis techniques" (Tucker et. al. 1999) or "partitioned into [...] constituent components based on surface types" (Perovich et. al. 2002).

To find out how to best recognise the melt ponds from my own set of images, I experimented with all three methods listed above: choosing a suitable brightness threshold level, taking advantage of the difference in between the blue and the red channels, and image classification. Image classification is the method I decided to use, and I will discuss it more closely in chapter 5.3. In this chapter I will briefly describe some of the other image partitioning methods and explain why I did not choose to use them.

Simply setting a suitable brightness threshold level was my first attempt. The method did not work with my data, at least not for the images taken on sunny days. The brightness values of shadow pixels are rather similar to pond pixels, and whenever there are shadows on the ice, they invariably get classified as ponds. The man-made

objects visible in the images, such as the riggings of the ship, are by far the darkest areas in the image. They also fall below any brightness threshold level chosen above the pond pixel brightness. The latter problem is not hard to go around: one can specify upper and lower threshold levels and discards the pixels that fall below the lower threshold or above the upper threshold. This works fairly well for dark and cloudy days, but I wanted to find a method that would not fail as the illumination increases.

Some examples of trying to separate the ponds with the help of two brightness threshold levels are shown in Figures 11–13. Figures 11, 12 and 14 are created by using a greytone version of Figure 10 (taken on 17. July 2007), and Figure 13 is created from a greytone version of an image taken on 16. July 2007.

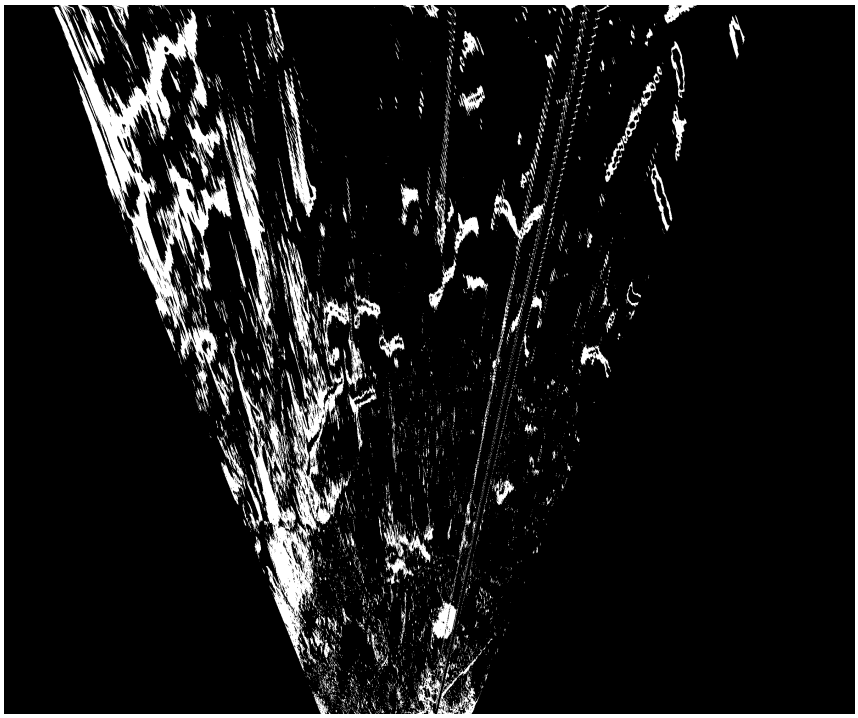

**Figure 11**: *17.7.2007 (a sunny day), lower brightness threshold set to 120 and upper brightness threshold set to 140.*

In Figure 11 I have set the lower brightness level to 120 (out of 255) and the upper brightness level to 140. All pixels that in a greytone version of Figure 10 fall within this brightness region are shown in white colour. The edges of the ponds are already

visible in white, but not the whole ponds. Even when the upper brightness threshold is set this low, there are a lot of shadows and some other darker areas on ice that fall into the chosen region.

In Figure 12 I have set the upper threshold as high as 150, to allow all parts of the ponds to become visible. As a result, most of the ice is coloured as white as well. There is no way of getting around this effect: the pond pixel brightness values do overlap with shadows and darker patches in the ice, and no such brightness region can be found as to only accommodate pond pixels.

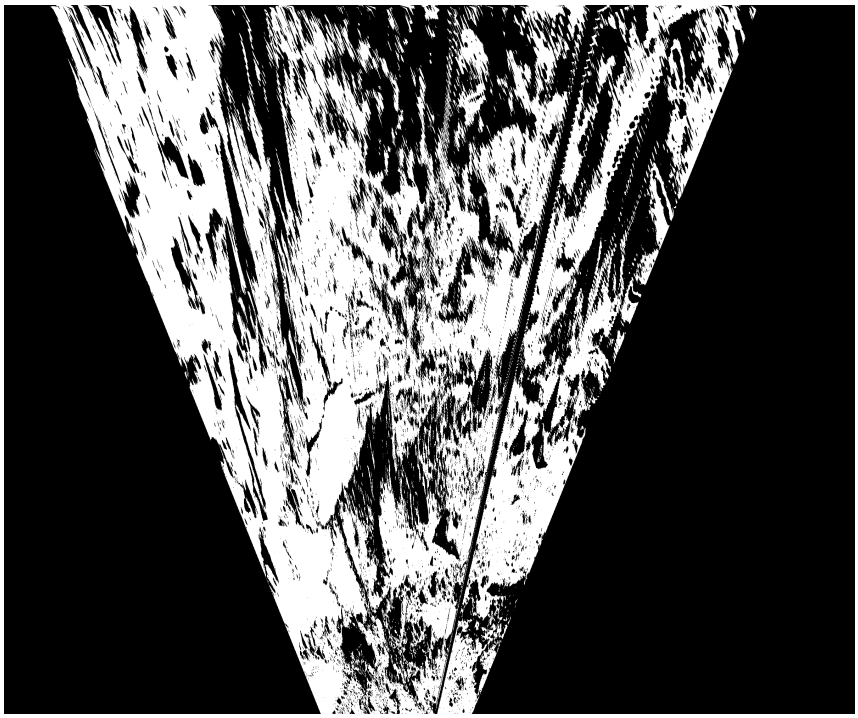

**Figure 12**: *17.7.2007 (a sunny day), lower brightness threshold set to 120 and upper brightness threshold set to 150.*

As pointed out before, this method works markedly better, if the image being analyzed is taken on a cloudy day. There are less hues of colour in the ice on cloudy days, the ponds make a sharper contrast with their surroundings, and there are no well-defined shadows to complicate matters. It is also important to bear in mind that illumination is not the only factor that changes in between the images. Poorer illumination is a result

of cloudier conditions, and near the North Pole, cloudy skies often snow. In my data set it is clear that during cloudy periods it has been snowing, and new snow in indirect sunlight is spectrally a lot more homogeneous surface than partly snow-covered ice on sunny days. That is part of the reason why ponds are easier to separate as their own brightness class (or, later, as their own spectral class) from cloudy images.

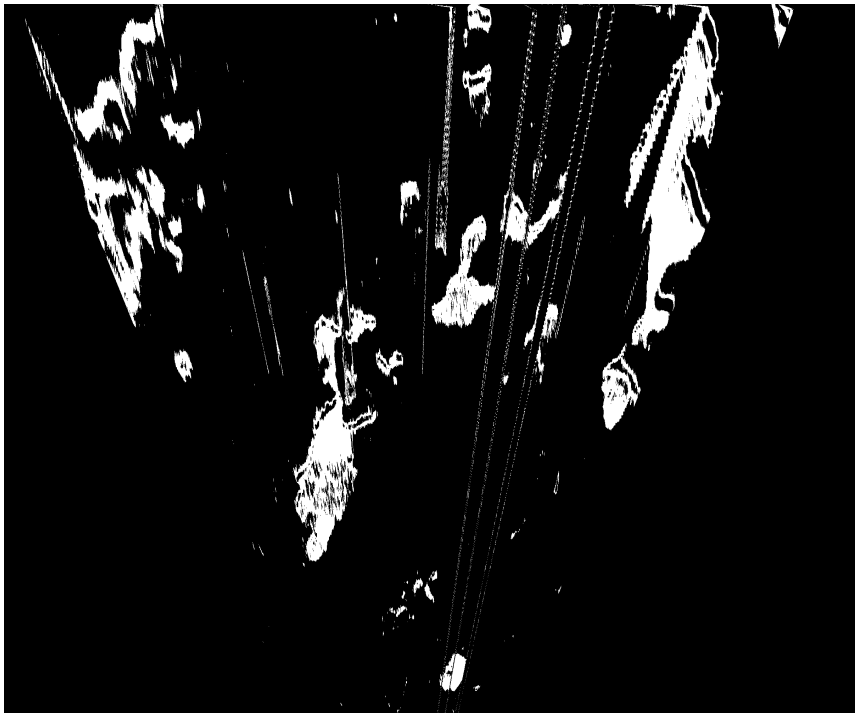

**Figure 13**: *16.7.2007 (a cloudy day), lower brightness threshold set to 120 and upper brightness threshold set to 140.*

Figure 13 is an image from 16. June 2007, which was a cloudy day. I have chosen the same brightness region to show up in white as in Figure 11, and the result is clearly much better. However, I wanted to find a method that would work with sunny images as well as cloudy ones, and therefore I found it necessary to explore other image partitioning tactics.

Melt ponds often have a spectral albedo that peaks in the blue wavelength region, as was shown in Figure 3. The melt ponds in my data certainly appear bluish, and I suspect their spectral albedo to be similar to curve f in Figure 3 (spectral albedo for

mature melt pond with blue bottom on multi-year ice). In Figure 14 I have plotted an RGB brightness profile across a melt pond seen in lower left part of Figure 10. The scale of brightness is from 0 to 255, although in this case the brightness values only range from about 80 to 200. Brightness values are plotted as a function of location (in this case, pixel). In physical world, the profile corresponds to approximately 3 metres on ice.

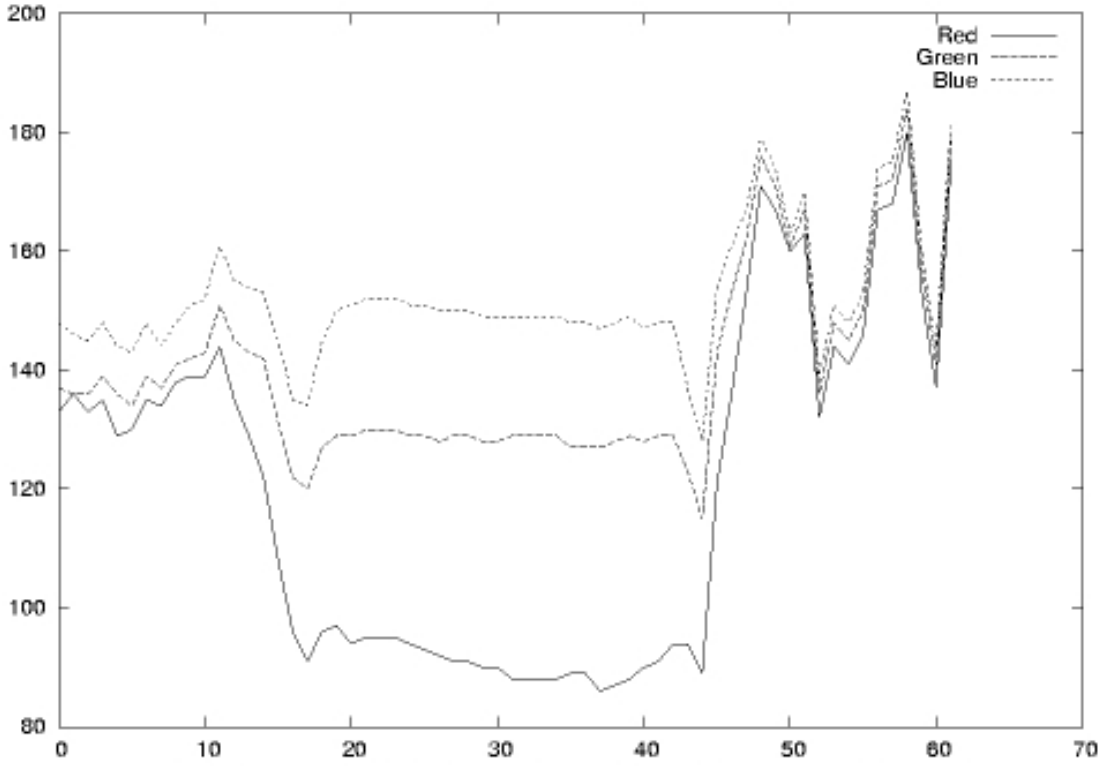


**Figure 14**: *Brightness values for red, green and blue channels in a profile across a melt pond in Figure 10.*

It is clear from the profile in Figure 14 that for pond site pixels the red channel is the weakest and the blue channel is the strongest. This is analogous with curve f in Figure 3: melt pond albedo peaks at blue wavelengths and diminishes towards the red wavelengths. The difference between the red and blue channels has been utilized in some studies. It is also evident that the brightness values of snow and ice pixels are by no means constant. This, in turn, is analogous to the fact that the snow and ice albedos do vary quite a lot according to surface type, also in the small horizontal scale.

Spectral albedos for different snow and ice types are, however, almost constant across the optical wavelenght range (see curves a and b in Figure 3), meaning that when there is a darker patch on the snow or ice, all channels (red, green and blue) will record lower brightness values. This is also seen in Figure 14: when the profile line intersects a pond, the three channels diverge, but are all three fairly constant all the way across the pond. When the profile cuts across ice surface, the brightness values vary a lot more, but all three channels change in almost the same manner.

Tschudi et. al. (1997, 2001) have used the difference in between the blue and red channels by subtracting the red channel from the blue, getting a greytone image as a result, and then selecting suitable brightness threshold values to define the pond sites. This approach works with my data fairly well, better than simply choosing the brightness threshold values from the greytone image. Figure 15 is again the same image as in Figure 10, with red channel subtracted from blue, and brightness values from 35 to 75 shown as white.

**Figure 15**: *17.7.2007 (a sunny day), red channel subtracted from the blue channel, lower brightness threshold set to 35 and upper brightness threshold set to 75.*

Figure 15 is already a rather successful attempt to separate the ponds from the ice, but clearly a lot of shadows are still classified as ponds. Other arithmetic operations on red and blue channels can also be tried, such as dividing the blue channel by the red channel. Some attempts work better than others, but my end conclusion on these tests was that I still needed to experiment with other techniques to find the best way to partition the images into ponds and other surface types. I was also concerned about the fact that choosing the suitable brightness thresholds separately for every image seemed a very subjective method, prone to errors of judgment.

## *5.3. Image classification*

After some experimenting, I settled on unsupervised classification as the best means of partitioning the Karhukamera images. Image classification is a procedure usually performed on images consisting of two or more bands: in this case, blue, green and red bands. Any pixel in such an RGB image can be thought as a spectral vector: a point in three-dimensional RGB-space. (It should be noted, that RGB is not the only colour model available, although it is the one used in this study.) (Landmark et. al. 1995, 75–84; Neteler & Mitasova 2002, 247, 252–253)

Image classification is done by finding a way to place spectral vectors into a given amount of separate clusters. These clusters are called spectral classes, and in remote sensing applications they usually correspond with different types of terrain. Separate land cover or land use categories – such as forest, field, rock, ice, sweet water, salt water, urban areas – all have a specific spectral signature, although some overlap may occur between the spectral signatures of different classes. (Landmark 1996, 75–76.)

It should be stressed that the wavelength bands used in image classification do not need to be red, blue and green, nor do they need to lie in the visible region at all; in

earth observation applications, they often don't. The wavelength bands being used in the analysis depend on the imaging instrument and the aims of the study. Both red and near-infrared bands are highly useful for vegetation mapping, for example (e.g. Neteler & Mitasova 2002, 237). Since water absorbs infrared radiation a lot more effectively than snow or ice, it might be a good idea to use an infrared band for the detection of ponds as well. My set of data, however, doesn't allow for that option.

Unsupervised classification can be performed by several different clustering methods, and various criteria can be used to evaluate the goodness of the clustering. One common clustering criterion is the Sum of Squared Errors (SSE), in this case obtained by calculating the average distance of vectors from the cluster centre for each cluster individually, and then adding up this measure for all the clusters. Minimizing this quantity leads to the clustered vectors being as close to their cluster centres as possible, which is a good measure of the successfulness of the clustering. (Landmark 1996, 84.)

My choice of clustering algorithms was limited to the ones provided in free software contexts readily available to my purposes. The two programs I mainly experimented with were OpenEV, which uses ISODATA-algorithm for unsupervised clustering (ISODATA stands for Iterative Self-Organizing Data Analysis Technique), and GRASS GIS, which has several supervised and unsupervised classification options. Both OpenEV and GRASS GIS are open source toolkits developed for processing geospatial information and freely downloadable from the Internet (OpenEV: http://openev.sourceforge.net, GRASS GIS: http://grass.osgeo.org).

ISODATA algorithm starts out by defining as many cluster centres as desired, based on the statistical properties of the samples, and then making an initial estimate as to which clusters the individual vectors should be placed. Then it iteratively rearranges the vectors, moving them from one cluster to another if needed, minimizing the SSE in

the process. (Landmark 1996, 84.) While this method provided promising results performed on the Karhukamera data – ponds could clearly be separated as their own spectral class, as long as a suitable number of classes was defined – the OpenEV program turned out to be rather slow, and the classification took far too much processing time.

I then switched into the open source GIS (Geographical Information System) GRASS, which proved to be more efficient platform for my purposes, and performed the classification faster. GRASS uses a two-step method for unsupervised classification: first one module (i.cluster) iteratively groups the data vectors into a user-defined number of clusters, and calculates the means and covariance matrices for each initial cluster. These will be the spectral signatures of each class.

The spectral signatures created by i.cluster are given as an input to another module, i.maxlik. This module uses an algorithm called Maximum Likelihood Classifier (MLC) for performing the final assignment of each image pixel into one of the spectral classes. MLC assumes that the pixels in each spectral class are distributed normally, and calculates the probability of each pixel belonging to one of the spectral classes created by i.cluster. The spectral class with the highest probability is chosen, and a classified image is created. The requirement that pixels in each spectral class should be normally distributed is not always met in practice, and when not, complications may ensue. (Neteler & Mitasova 2008, 316–317.)

The methods described above are examples of unsupervised classification. Another classification approach is called supervised classification, and refers to a process where the spectral signatures of each terrain class are not created wholly automatically from the data. The person or persons performing the classification may, for example, choose some well-defined training areas from the images being classified, and then specify the

spectral classes based on the distribution of pixels included in those training areas. In an ideal situation, the training areas are chosen not only based on how an image looks, but with the help of some additional data about the area. If, for example, an area in the image has actually been visited, or its characteristics have been measured by some other instrument, its terrain type may be confirmed. Obtaining this kind of "ground truth" is important, because it is really the only way to reliably assess the goodness of the classification. (Landmark et. al. 1996, 76–81; Neteler & Mitasova 2008, 319–322.)

Searching for the best classification methods for the Karhukamera images, I experimented with supervised classification as well as unsupervised. Although I don't strictly have the ground truth concerning my chosen spectral classes, it is still fairly easy to spot some good training areas from the images, and claim with reasonable accuracy that the terrain type in a chosen training area is known. With my data and the GRASS software I could, for example, choose a training area encompassing only pond pixels, another encompassing only grey ice pixels, yet another encompassing only bright snow pixels, and so on. Then GRASS can compute the distribution of pixels in each training area, and have those distributions define the required spectral classes. The spectral classes thus obtained are given as an input to the MLC algorithm to create the final classified images.

Yet another classification approach is to combine both supervised and unsupervised classification. With GRASS this can be done, for example, by first choosing the training areas, and then giving them as an input to the clustering algorithm. The algorithm will take the predefined spectral classes into account, as it starts the iterative process of grouping the image data into clusters. This may help the clustering algorithm to perform better, and to end up with just the desired land use classes. The obtained spectral classes are again given as an input to the MCL algorithm, which will produce the final classified image. (Neteler & Mitasova 2008, 322.)

Having tried both supervised and unsupervised classification procedures, as well as their combination described above, I have chosen unsupervised classification as the method most suited to partition my images into distinct surface classes, one of them being the melt ponds. It must be stressed, that in this study the goodness of the classification cannot be estimated otherwise than by comparison with the original images. This is unfortunate, but cannot be helped, since there is no additional data to be had for comparison purposes. The albedo measurements done near *Tara* might be useful in this respect, since the temporal evolution of the albedo correlates with the growth of melt pond coverage. However, the albedo data is not yet available for comparison.

The lack of any reliable way to affirm the ground truth is not just the problem of this study, however. I have referred to several melt pond coverage studies in chapter 3.3, and mentioned some of their image partitioning methods in chapter 5.2. It seems to me that there commonly is no independent way to establish the goodness of the classification, so it must be done by looking at the original images and comparing them with the classification results. The problem of this approach is that it is difficult to estimate the error of the results. As long as the goodness of the classification is for the researcher alone to decide, there will always be errors of judgment inherent in the process of choosing the best classification results, and those errors are hard to quantify. It is not possible, in fact, to estimate the absolute error in the melt pond percentage, if no additional data exists for this purpose. I will look more closely on the error estimates in the next chapter.

Changes in illumination conditions change the way the ice looks in the images, and bring about a different number of required spectral classes. For cloudy images, only 3 or 4 spectral classes were sufficient, whereas for sunny images, as many as 8 spectral classes were needed. This was mainly due to the fact that blue melt ponds were rather

difficult to distinguish from the bluish shadows in the ice present on sunny days. There needed to be enough spectral classes so that shadows and melt ponds would both fall into their separate classes, and not into the same class.

Not even the supervised or partly supervised classification approaches could help with the distinction of ponds and shadows. I tried choosing separate training areas from shadows and ponds, but even this didn't bring about a clearer separation of pond and shadow spectral classes in the final classified image. I must conclude that this difficulty cannot be overcome by choosing a different classification approach. It is a real effect of optics that both melt ponds and shadows appear bluish against snow, and it seems there will be overlap in between their spectral classes, however carefully the spectral signatures of different classes may be created. The best result I could get was always one where some shadow pixels were classified as ponds, and seemingly an equal amount of pond pixels were classified as shadows.

Fetterer and Untersteiner (1998) point out that there is some overlap in between wet summer ice and melt pond spectral classes, but since the albedo distributions for both classes are equally broad, it is possible to perform the classification so that the number of ice pixels misclassified as pond is as large as pond pixels misclassified as ice. This is the same result I hope to have achieved concerning the separation of ponds from ice, as well as the separation of ponds from the shadows.

Yet another problem was that some of the riggings of the sail ship *Tara* are visible in every image. The ropes stand in stark contrast against the snow and ice, and with a suitable amount of spectral classes chosen, they will form their own spectral class. However, a thin line of pixels around the edges of the ropes is persistently classified as pond pixels, no matter which classification scheme is used. I believe this to be an effect created by the camera or perhaps the compression of the picture file, not a real

physical effect like in case of pond and shadow pixel distributions. Rope pixels seem much darker than pond pixels, and no rope pixels from the middle of the ropes are ever classified as ponds, just the edges of the ropes. However, the ropes usually cover no more than 1% of the whole area of the image, and their edges cover yet a smaller area, so no very great error occurs from the classification of rope edges as ponds.

I tried to reduce the rope edge effect by removing the ropes from the images altogether. Since ropes are the darkest objects in the picture, this can be done by simply setting all pixels below a certain brightness threshold as null, containing no data. This proved to be a bad idea: if the brightness threshold value was set high enough to mask the confusing rope edges, some pond pixels were lost as well. This was, of course, only to be expected. And if the ropes were masked only to the extent that all pond pixels stayed untouched, the confusing rope edges remained. The best result that could be hoped for was one where the ropes all fell into one spectral class, leaving only a faint trace of rope edge pixels classified as ponds.

Figure 16 is an unsupervised classification, again done with the image from 17. July 2007. The pixels classified as riggings have been coloured black, and the ponds are shown as blue. All the rest is different types of ice and snow.

The problem with the shadows being classified as ponds has indeed been solved to some extent; now mainly the edges of shadows get classified as ponds. Some pond edges are also not recognized as ponds, but this may actually bear some physical meaning: there may in fact be new ice forming along the edges of the ponds, although this is hard to confirm just by looking at the original photographs.

A classification of an image taken on a cloudy day (16. July 2007) is shown in Figure 17. On a cloudy day, the shadows do not complicate matters, and the resulting

classification seems more accurate than one done on a sunny image. However, in the cloudy image classification, some dark areas of the ponds are placed in the same spectral class as the ship riggings. Classification is by no means a perfectly accurate method of partitioning the image into different surface types. Although the goodness of the classification cannot be established without some other data to compare the results with, I can and do know that some pixels have been misclassified in every classification attempt I've made.

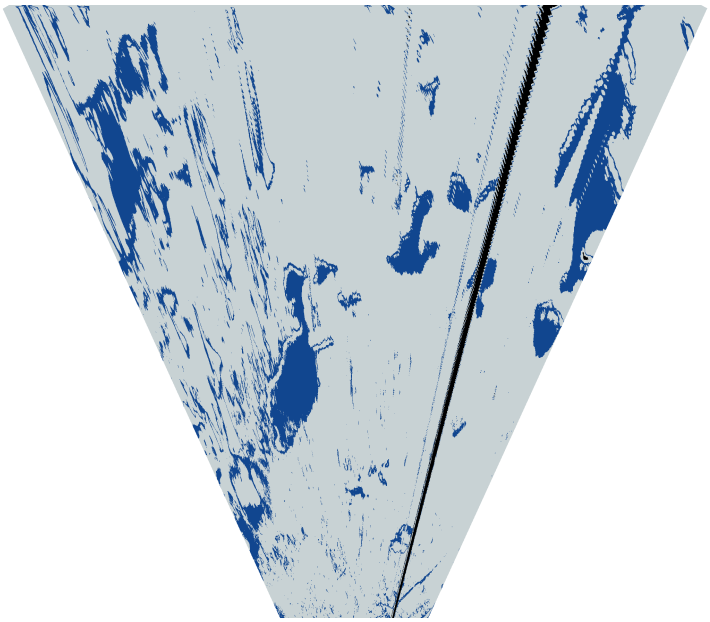

**Figure 16**: *17.17.2007 (a sunny day), unsupervised classification done with 8 spectral classes.*

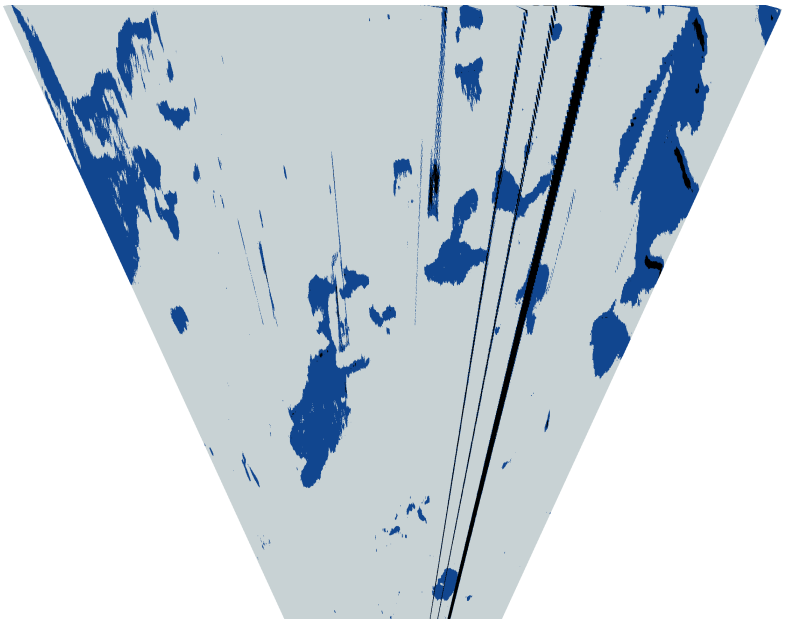

**Figure 17**: *16.17.2007 (a cloudy day), unsupervised classification done with 4 spectral classes.*

It was mentioned in the previous chapter that choosing the suitable brightness thresholds for every image seems like a very subjective process, easily affected by the researcher. Choosing a suitable number of spectral classes is, of course, not a wholly objective exercise, either. However, I feel like the connection in between real physical effects and the resulting classified image is better preserved in the classification method. If the number of spectral classes chosen corresponds in some reasonable way with the number of terrain types actually captured in the images, the resulting classification will seem sensible. Although the amount of spectral classes needed to be adjusted, as the illumination conditions and other physical factors (such as the amount of fresh snow on the ground) varied, I still felt this was a process less prone to errors than tweaking the brightness thresholds for every image separately.

# 6. Results

I have obtained the melt pond coverage from 22 days during the data collection period. Only one classified image per day is attempted, and all the chosen images are taken at local noon, so that the illumination conditions might vary as little as possible. The camera unit has been active from 22. April, but the first signs of melt ponds appear almost 2 months later, 19. June. The melt period captured on the camera unit is therefore only 33 days long. The camera stopped functioning early in the morning of 22. July, so no noon image could be obtained from that day.

As described in chapter 5.1, in order to perform the perspective correction for an image, one needs to give the tilt of the horizon as a correction parameter. The summer season 2007 near the North Pole seems to have been cloudy, foggy and rainy, which means that the horizon is often not discernible in the images. As long as the ship has not been shifting her position, it is often possible to correct even some of the foggier images by taking the correction parameters from the preceding or following image. If the ship and the camera have moved in between the clear day and the foggy day, this is no longer possible. On some days the rain drops or sleet on the camera casing effectively block the view, and those days have been left out of the analysis as well. All in all, six days have been left out for these reasons: 1.–4. July, 6. July and 18. July.

The first faint traces of melt ponds are seen on 19. June, and they have grown slightly larger the next day, 20. June. The first clear features that look like actual melt ponds, albeit very little ones, appear on 21. June. The two tiny ponds are too small to be distinguished as a separate spectral class, so no accurate melt pond coverage is obtained for 21. June. The area covered by ponds on that day is in any case small, less than 1%. On the next day a tarpaulin comes loose from the riggings of the ship and

hangs in front of the camera for several hours. The noon image cannot be used; in fact, the next useful images is obtained more than 11 hours later.

However, even the next day, 23. June, the melt ponds are so small that they don't form a spectral class of their own. It's not just a question of area, since the ropes do form their own spectral class, although they only cover about 1,5% of the image. The ropes, however, stand in stark contrast to other features in the image, whereas young, barely formed melt puddles are almost the same colour as wet, slushy snow. Of course, very young melt puddles *are* just patches of slushy snow; there can be no absolute definition as to when an area is still wet snow and when it has become a young, shallow, slushy melt pond. This makes the classification difficult, when very young melt ponds cover only 1%–2% of the image.

The first actual result is obtained from 24. June, when the melt pond coverage has reached approximately 3%. The camera was operational until early morning of 22. July, which means that I have been able to obtain melt pond coverages from a period of 28 days. Out of those 28 days, melt pond coverage has been calculated for 22 days. The classified images from those days are shown in Figures 18–39. Spectral classes corresponding to ponds (blue) and ropes (black) are shown separately, and all other spectral classes corresponding to different types of snow and ice are merged together.

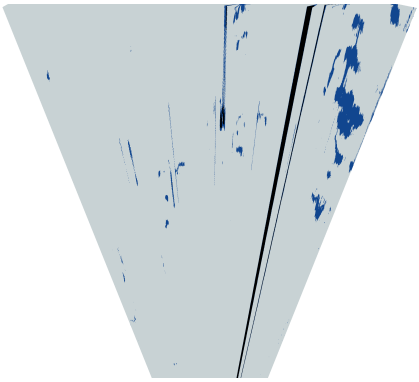

**Figure 18**: *24.6.2007*

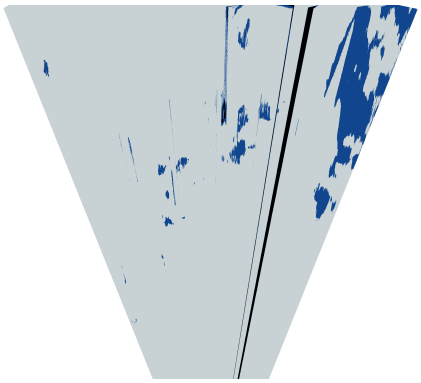

**Figure 19**: *25.6.2007*

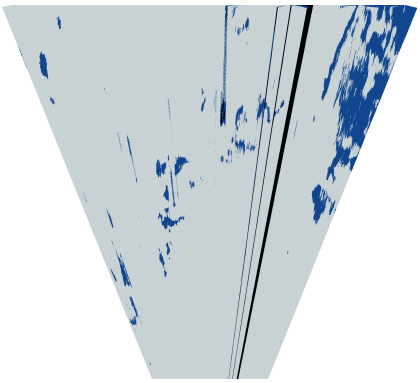

**Figure 20**: *26.6.2007*

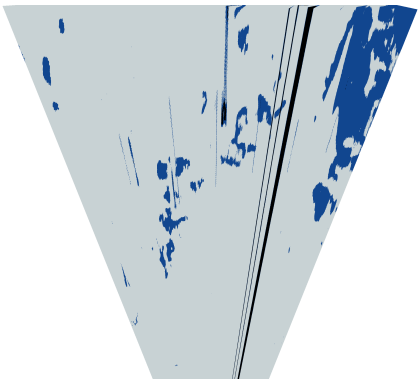

**Figure 21**: *27.6.2007*

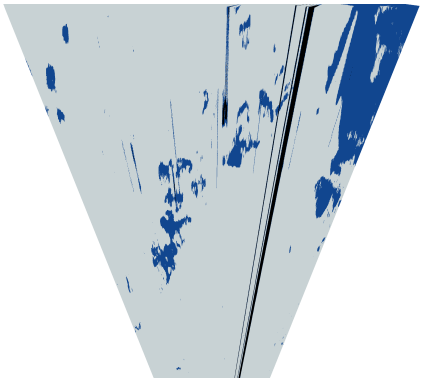

**Figure 22**: *28.6.2007*

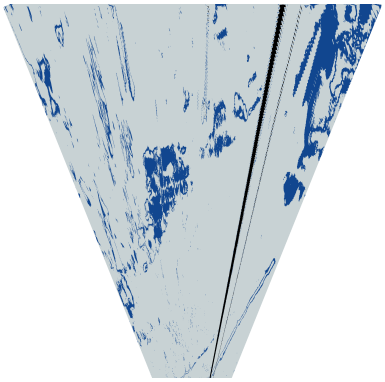

**Figure 23**: *29.6.2007*

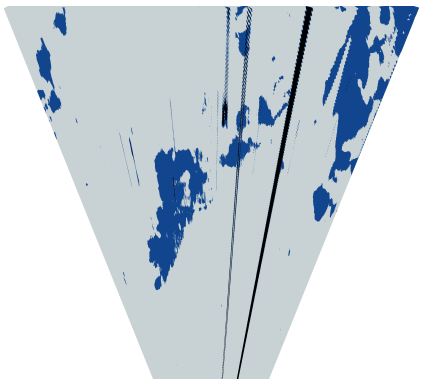

**Figure 24**: *30.6.2007*

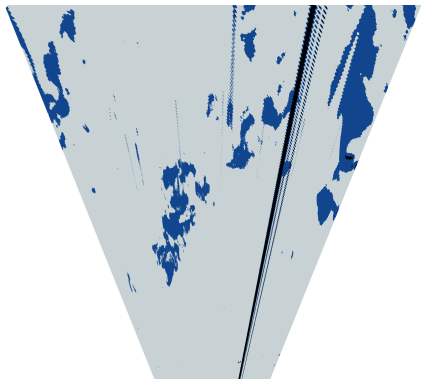

**Figure 25**: *5.7.2007*

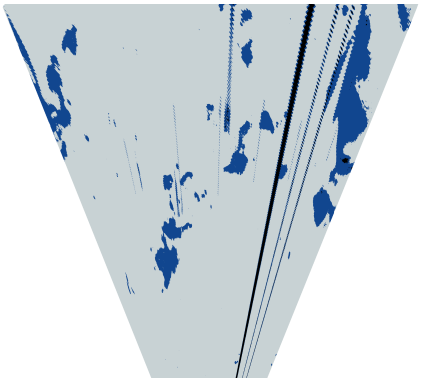

**Figure 26**: *7.7.2007*

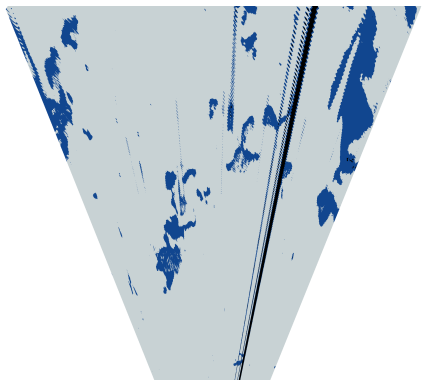

**Figure 27**: *8.7.2007*

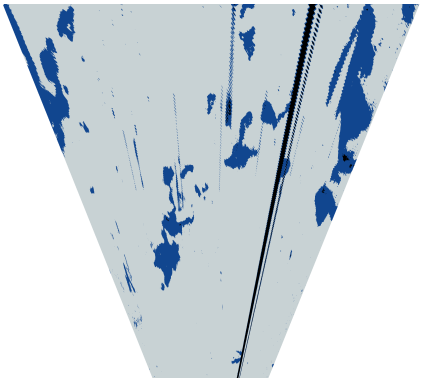

**Figure 28**: *9.7.2007*

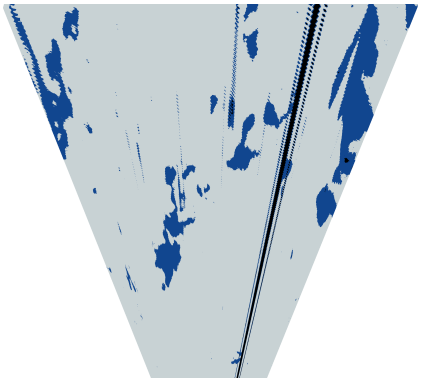

**Figure 29**: *10.7.2007*

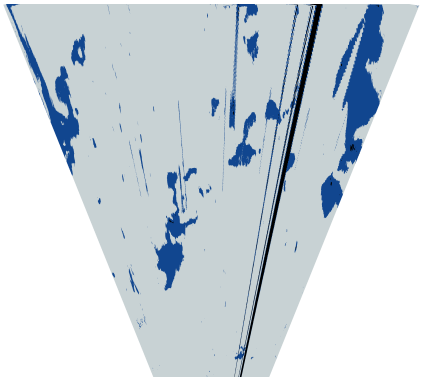

**Figure 30**: *11.7.2007*

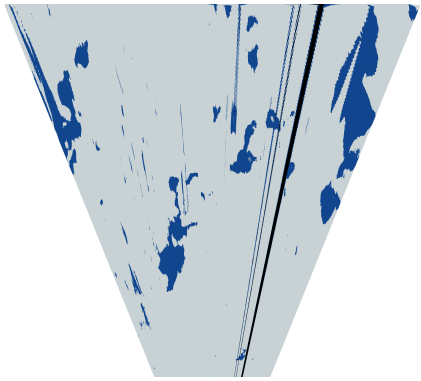

**Figure 31**: *12.7.2007*

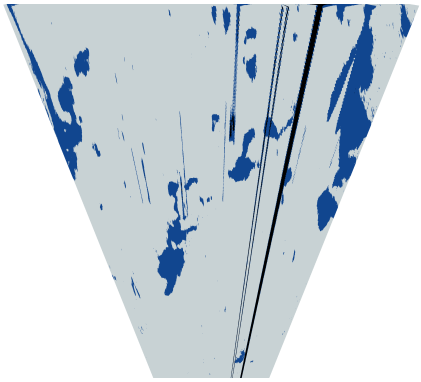

**Figure 32**: *13.7.2007*

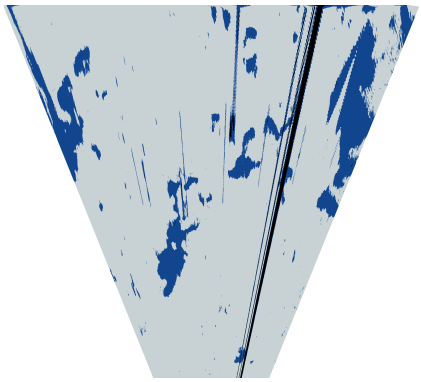

**Figure 33**: *14.7.2007*

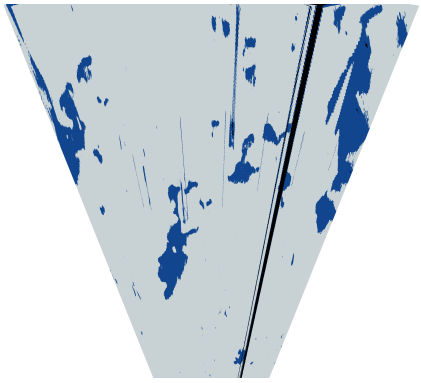

**Figure 34**: *15.7.2007*

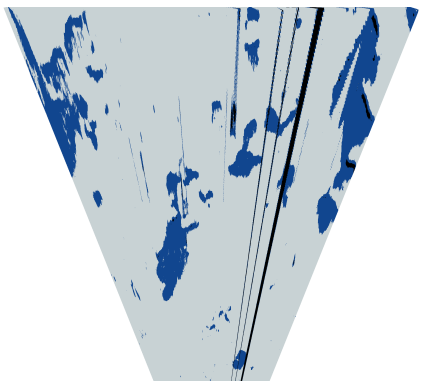

**Figure 35**: *16.7.2007*

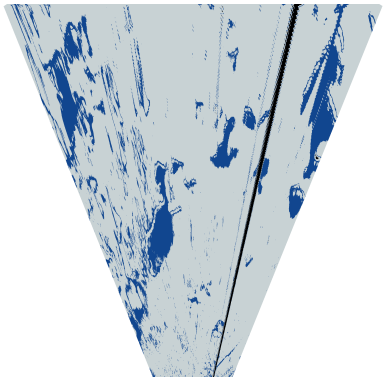

**Figure 36**: *17.7.2007*

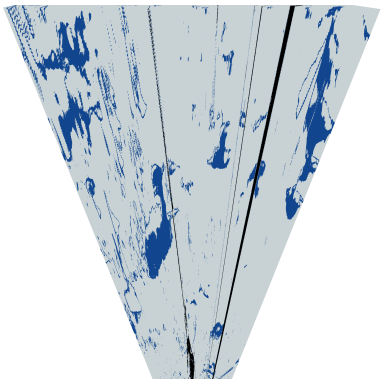

**Figure 37**: *19.7.2007*

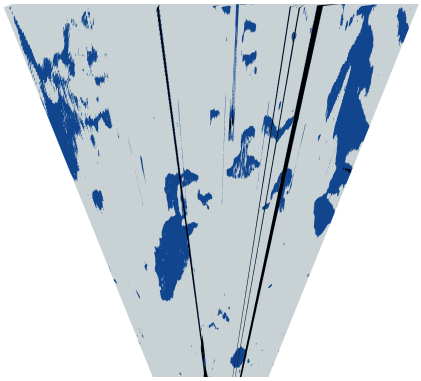

**Figure 38**: *20.7.2007*

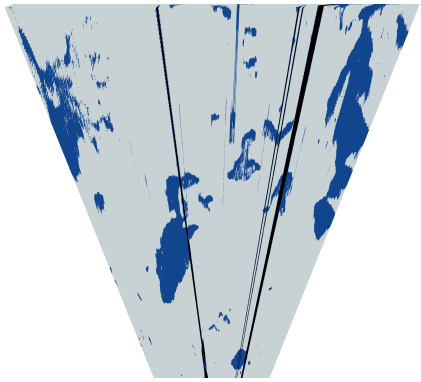

**Figure 39**: *21.7.2007*

Figure 40 shows a time series of the melt pond fraction, calculated from the classified images shown in Figures 18–39. The result from sunny days are plotted with red, to stress that they are the least accurate data spots.

Although the very onset of melt is not covered by this time series, my estimate based on the pertaining images is that the melt pond fraction increases from 0% to 3% in five days (20. June to 24. June.). During that time, the melt pond fraction grows by approximately 0,6% every day. From 24. June onwards, the growth rate more than doubles. Melt pond fraction increases from 3% to approximately 14% in seven days, totalling a daily increase of 1,6%.

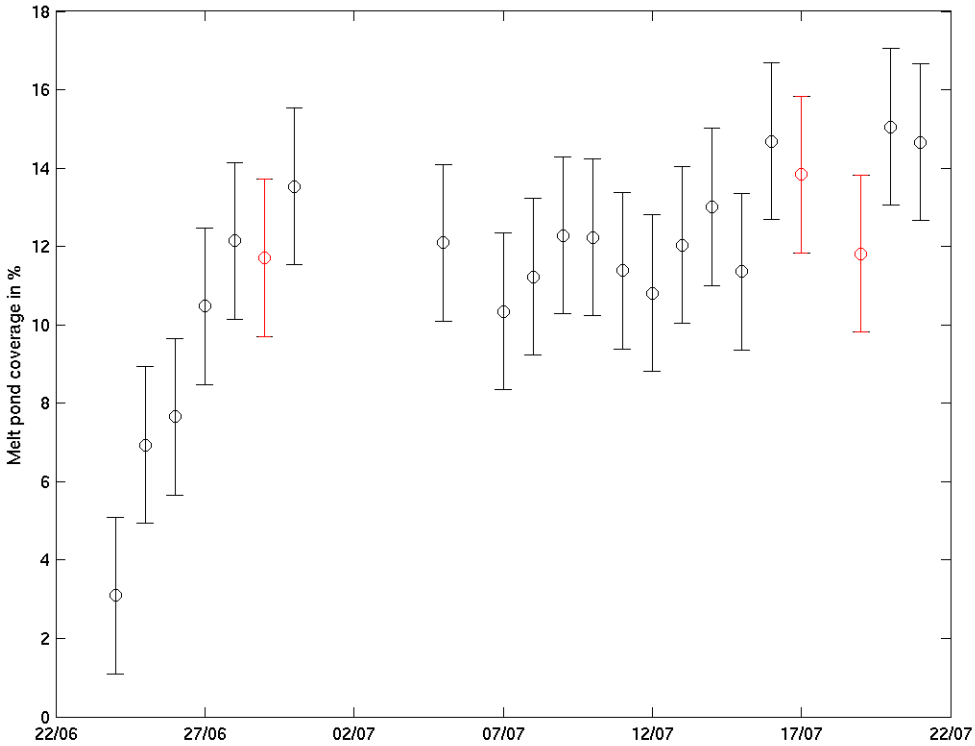


**Figure 40**: *Melt pond coverage near Tara from 24. June to 21. July.*

After 30. June there's an unfortunate gap in the data: images from 1. July to 4. July could not be geometrically corrected due to foggy conditions. Images from those days are still clear enough to form an estimate that the rapid phase of the melt does end on 30. June. The melt pond fraction stops growing significantly, and instead starts oscillating around 12% for approximately two weeks (1. July to 15. July). After that, the melt pond coverage increases slightly and reaches the vicinity of 15% by the end of the data collection period (21. July).

I have estimated the error in calculated melt pond fractions to be ±2%: that is, any given percentage is inaccurate by ±2 in percentage units (as opposed to the relative error being only 2%, which is not the case here.) It is important to stress that I have no reliable way of estimating the absolute error made in calculating the melt pond percentage, at least without any auxiliary data (e.g. satellite images or albedo measurements) to compare my results with. My current estimate of error has more to

do with the classification process itself; more specifically, the reproducability of my results. When performing classifications on my images, I judged the goodness of the classification by comparing the results with the original images. It was clear that a well-premeditated choice of parameters was needed for the classification to succeed at all, the most important parameter being the number of spectral classes chosen. By changing the amount of spectral classes chosen, I could often produce more than one result that looked reasonably good, compared with the melt pond distribution apparent in the original image.

The classification approaches and the parameters I have ended up using are the ones I have judged best, and the errors inherent in this kind of judgment are impossible to quantify. However, all the results that looked reasonable did fall within ±2% of the result from the best classification attempt, and hence my choice of ±2% for the error estimate. When assessing the errors inherent in the classification process, I used the OpenEV programme as well as GRASS, to perform a double check on the results. The melt pond fractions obtained from the best-looking classifications did fall inside the ±2% margin even when the classification was performed with another programme. I also did some checks by using the alternative image partitioning methods mentioned in chapter 5.2, and their best results fell into the same ±2% margin.

The final error estimate is made with an image from a sunny day, and as has been pointed out before, the classification of sunny images was a lot more prone to errors than the classification of images taken on cloudy days. The error estimate done using a sunny image, ±2%, should therefore more than cover the errors made in classifying the images taken on cloudy days.

There are multiple sources of error inherent in the image correction process, as well as in the classification itself. The correction parameters have been selected from images

by hand, which means they can hardly be absolute. However, by comparing all rectified images with each other, it seems that the same area is captured in each consecutive image with a reasonable accuracy. Moreover, I have discarded the images that could not be reliably corrected. I suspect that the error due to the correction being a slightly inaccurate process are covered by the ±2% error estimate.

There is also a type of inaccuracy that rises both from the image correction procedure and the circumstances prevailing on the ice. The ice surface is far from smooth; there are protruding features ranging from ice ridges to small piles of snow. Since the images used in this study are not aerial images, higher parts of the ice field may block some other, low-lying features from the view of the camera. I have not even attempted to estimate the error that might be caused by this effect, since a reliable estimate would require detailed knowledge of the ice topography on the site. I admit such errors may be inherent in the results, but I cannot claim to know how large they are.

# 7. Discussion

## 7.1. Comparison with previous results

It is not easy to compare the actual melt pond fraction with previous studies, for reasons that are immediately apparent from Table 1 and have already been discussed in chapter 3.3. The majority of previous melt pond coverage measurements have been made at different times and different locations than the ones this study concerns. My results start 24. June when *Tara* was at 88°11' N, 124°20' E, and end 21. July at 87°56' N, 43°16' E (see Figure 7), and there is very little pond coverage data from that far north.

That being said, the results presented here seem to be in broad accord with several other pond coverage figures presented in literature. Perovich et. al. (1997) obtained a pond coverage of 12% in July 1994, at 76°N; El Naggar et. al. (1998) obtained a pond coverage of 19,0% ± 6,85% on multi-year ice in July 1993 at 78°N; Tucker et. al. (1999) obtained a pond coverage of 12% in July 1994 at 76°N, 3% in August 1994 at 84°N and 0% in August at 88°N; Tschudi et. al. (2001) obtained a pond coverages from 24,6% ± 6,2% to 34,1% ± 8,4% in July 1998 at 78°N; and Perovich et. al. (2002) obtained pond coverages from 17% to more than 20% in July 1998 at 78°N. (See Table 1 for details.)

The melt pond coverages obtained at latitudes 76°N and 78°N are not far from my result of 0% to 14% in June and 12% to 15% in July. This is perhaps surprising, since one would expect the pond coverages obtained at 88°N to be considerably smaller than those measured at the same time of the year and some 10° to the south. The northernmost previous results are presented by Tucker et. al. (1999). They are from

August, so I cannot compare them directly with my results. However, I will attempt a comparison at the end of this chapter, after I have discussed the temporal evolution of melt ponds near *Tara* through the summer 2007 with the help of some additional data.

The type of temporal evolution of melt pond fraction plotted in image 40 has been observed in some previous studies. Quoting from Perovich et. al. (2002): "In mid-June ponds cover a few percent of the ice, but then, in just a few days, between 15 and 18 June, [pond fraction] jumps by a factor of five from 0.04 to 0.20." This is very much in accord with the temporal evolution observed from Karhukamera data: the pond fraction increases by approximately a factor of 4,5 (from 3% to 14%) within a week. The rise in melt pond fraction observed in this study happens a bit later (starting from 24. June instead of 15. June) and is not quite as rapid as in the study done by Perovich et. al., but the melt pond fraction definitely exhibits a similar behaviour.

Also Derksen et. al. (1997) have reported similar results, obtained from a study area on ice as well as from aerial photos: "In a relatively short period of 10 [days], a sea-ice surface with no melt features and a spatially consistent late winter albedo was transformed to a surface composed of both water and snow, and a spatially erratic albedo influenced by their different absorptive properties." This is, again, in accord with the results from *Tara*. The first actual ponds are visible in images obtained 21. June, and by 30. June the pond fraction has reached the value of 14%, after which the growth of pond coverage slows down significantly.

It is no surprise that the pond fraction should rise rapidly soon after the ponds have first started forming; the physical explanation for this phenomenon was already touched upon in chapter 3.1. When the wet snow on top of the ice starts melting, there is a rapid influx of water from the melting snow. This water will form melt pools, usually located in the depressions on the ice. The ponds have a lower albedo than the

ice that surrounds them, and thus they absorb more heat. The melt rate of ice beneath the ponds is 2–3 times higher than that of the ice surrounding the ponds, which means that once the ponds have formed, the ongoing melt tends to take place under the melt pools. In this way, the ponds may continue to grow deeper as the melt season progresses, but they do not necessarily grow larger in diameter. (Fetterer & Untersteiner 1998)

Fetterer & Untersteiner (1998) point out that as the melt season progresses, the ponds that melt their way through the ice may actually start to shrink in diameter. Perovich et. al. (2002), on the other hand, have reported that even after the first rapid melt pond formation, the ponds continue growing wider, albeit at a slower rate than in the beginning. This latter result is in accordance with the melt pond fraction behaviour shown in Figure 40. Pond area seems to increase even after the very rapid phase of the melt, although the ponds do shrink intermittently. These oscillations seem to be driven by the local weather: when it snows heavily, the melt pond fraction goes down, since the ponds are partly snowed in. After the snowfall there is more wet snow on top of the ice, which may again melt and feed the existing melt ponds.

As the melt season progresses, the ponds eventually eat their way through the ice, and meltwater starts to drain through the ice into the sea below. More channels may also form in between the ponds and facilitate the runoff of melt water towards the edges of ice floes and into the sea. Thus the melt pond fraction is expected to diminish later on in the melt season. Indeed, Perovich et. al. (2002) have reported of a very rapid melt pond fraction shrinkage, as rapid as the initial growth of the ponds in the early season. Unfortunately my data results end on 21. July, and I have not much evidence as to how the melt pond fraction behaves near *Tara* during the late melt season. I suspect, however, that the maximum melt pond fraction was not yet reached by 21. July. I base

my estimate on some auxiliary data that I do have at my use, although not in an ideal form.

Figure 41 shows snow depth data from the snow depth measurement poles near *Tara*. From altogether nine poles I have chosen six that are visible in the Karhukamera images. It should be noted that the snow depth data is still unprocessed: what is presented here is the actual readings from the snow stakes. The data is courtesy of DAMOCLES campaign and at the time of writing, I don't have the means to convert the snow stake readings into the physical snow depth (i.e. the information about the initial position of the poles in the ice, which is needed to transform the stake readings into actual snow depth).

Even without being corrected, the snow stake readings give an accurate idea of how the snow level has been changing throughout the summer. When a snow stake has been standing in a melt pool, the snow stake reading records the water level; those data points are plotted with a star. Pond coverages from Figure 40 are plotted along with the snow stake measurements for comparison.

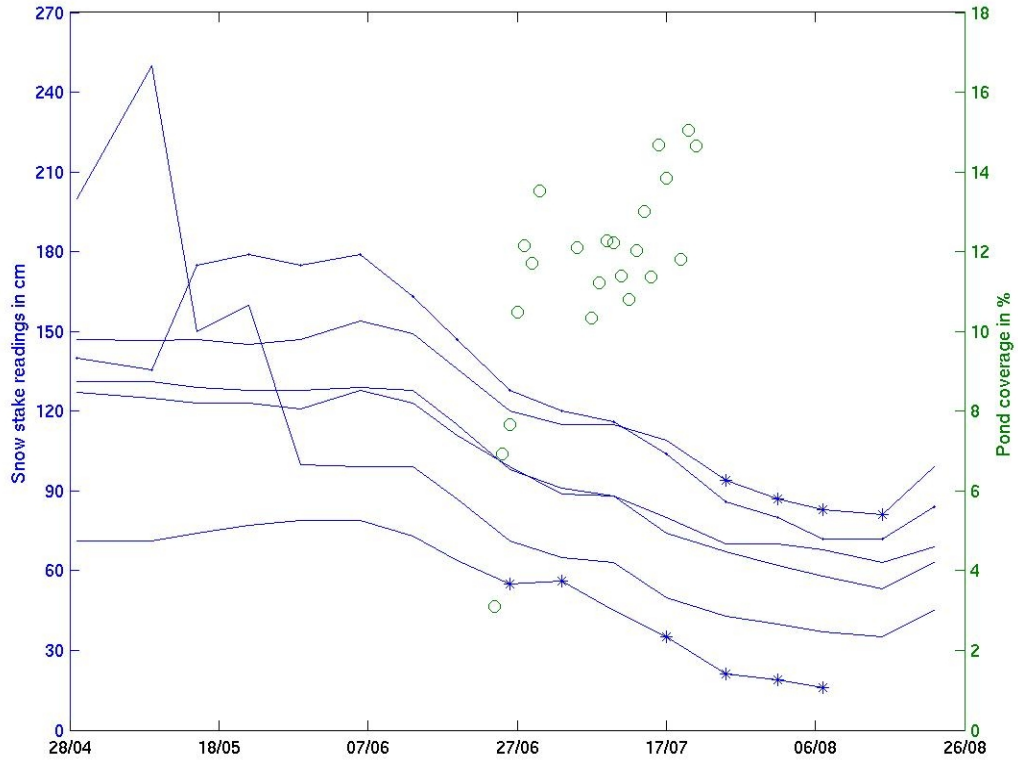


**Figure 41**: *Snow stake recordings from near Tara, 29. April to 22. August 2007.*

According to snow stake readings, the overall snow level starts to diminish rapidly around 6. June. The first actual melt ponds appear in the Karhukamera images on 21. June, 15 days later. According to my results, the melt pond coverage increases sharply from 21. June to 30. June. This is reflected in the snow stake readings: one of the chosen six snow stakes is already standing in a melt pool on 26. June. Interestingly enough, at the same time the decrease of snow level slows down somewhat. From 26. June onwards the snow level starts to diminish more gradually than it did in between 6. June and 26. June. This is, again, in accord with theory: after the first rapid phase of pond formation, melting tends to go on underneath the ponds, and the melting of the snow and ice around the ponds is not quite as fast as before.

It is worthwhile to note that even the snow stake poles situated in a melt pool show diminishing water levels; in fact, the water level in the ponds seems to go down at the

same rate as the snow level around them. This may indicate that there is some drainage going on, either along the channels connecting ponds with each other, or down through the ice. However, the snow stake data has not been corrected yet, and it is too early to arrive at any firm conclusions about drainage based on the data shown in Figure 41.

The snow level starts rising again on 15. August; at least it has risen from 15. August to 22. August, when the snow depth measurement period has ended. Based on both melt pond coverages and snow stake readings, it seems likely that the maximum melt pond coverage was reached sometime between late July and mid-August. This estimate is backed up by Figure 42, which is a photo taken from the mast of *Tara* on 20. August 2007.

**Figure 42**: *Melt ponds photographed from the mast of Tara on 20. August. (Photograph: courtesy of Tara Expeditions.)*

I don't know from which height the photo in Figure 42 has been taken, so I have no means to perform geometric corrections on it. By applying the classification algorithms to the image as it is, I obtained a melt pond coverage of 37%. This result is not strictly comparable with the ones presented before, since the data is different and has not been adequately pre-processed. However, 37% is a good estimate of the melt pond coverage at the time when Figure 42 was taken. Ponds are distributed on the ice

rather evenly, which also indicates that the obtained melt pond fraction of 37% probably isn't far from the truth, even though the image has not been geometrically rectified.

If the melt pond coverage did peak sometime before mid-August, and assuming that the 37% pond coverage estimate for 20. August is justified, the maximum melt pond coverage must have been more than 37%. Although I lack sufficient data for a better estimate, it is interesting to compare this figure with the study by Tucker et. al. (1999), which I already mentioned in the beginning of this chapter. Tucker et. al. found that on 13. August 1994 the pond coverage was 3% at 84°N, and on 18. August 1994 only frozen ponds were present at 88°N.

*Tara* was at 86,9°N on 20. August 2007, and whether or not the estimate of 37% pond fraction is correct, it is still clear from Figure 34 that ponds have been aplenty around *Tara* at that time. This result does not seem to compare at all with Tucker's. It should also be stressed that pond coverages obtained in this study seem to compare most favourably with those obtained at the same time of the year but some 800–1000 km to the south.

It is well known that there is a persistent trend of sea ice extent diminishing, most likely connected with the the global climate change driven by human-induced greenhouse gas emissions. Although the main results of the DAMOCLES campaign on board *Tara* have not yet been published, the preliminary results show that in September 2007 the measured Arctic sea ice extent was unprecedentedly low, only 4 million $km^2$. A major feature contributing to the exceptional ice conditions measured during year 2007 was a sea level pressure anomaly over the coast of northern Alaska and Canada. The cloud coverage over the Arctic was also lower than normal, and the

increased downwelling radiation may have caused the Arctic sea ice to melt more than usually. (Döscher et. al.)

The exceptional conditions of summer 2007 may be reflected in the melt pond coverage results presented in this study, especially through the comparison of my results with previous studies. However, without more DAMOCLES data from the year 2007 being published, it is difficult to take the analysis further. And moreover, the only previous pond coverage result from approximately the same latitude is from year 1994, and comparison with one previous year only is not extensive enough to warrant any far-reaching conclusions. It also needs to be taken into account that local anomalies may be reflected either in this study or the previous ones.

## *7.2. Conclusions and suggestions for future campaigns*

All in all, the effort to extract melt pond coverages from the Karhukamera data set obtained from near *Tara* proved to be successful. Melt pond fractions were calculated for 22 days, and the observed temporal evolution of the melt pond coverage agrees well with previous studies, such as Derksen et. al. (1997) and Perovich et. al. (2002). The obtained values of melt pond coverage seem high in comparison with Tucker et. al. (1999); in fact, they compare more favourably with studies done in much lower latitudes (76°–78°N as opposed to 88°N). This may be a consequence of exceptional weather and ice conditions in the Arctic during the summer 2007.

It is a pity that due to technical difficulties images could not be obtained after 22. July; the further evolution of melt pond fraction would have been of interest as well as the early melt season processes. However, the four weeks covered by this study is already

a reasonably long time span, certainly long enough to capture the rapid phase of the melt and to establish the following period of gradual melt pond growth.

The main motivation behind this study was the relation of melt pond coverage and sea ice albedo during the Arctic summer. Melt pond coverage is an important factor regulating the summer sea ice albedo, which in itself is one of the key parameters in the modelling of climate. Unfortunately, the albedo data measured at *Tara* is not yet available in a corrected form for the purposes of the study at hand. I cannot perform any comparison with the obtained melt pond coverages and the albedo measurements; it is a pursuit to be left for later. After the albedo data has been pre-processed, I believe the obtained time series of melt pond coverages is long enough for a meaningful comparison.

Should a similar data set be obtained in the future, for the purpose of observing the melt pond coverage, it can only be hoped that data can be acquired from throughout the melt season. If a camera is to be mounted in a mast or a tower, it is vital that the camera stays at the same height throughout the period of data collection. If that is not possible, it should be made sure that there are some kind of landmarks in the field of view of the camera, to be used for calibration purposes later on. In case images are obtained from a balloon, an aeroplane or a helicopter, the geometrical correction of the data should be a lot less difficult.

It should also be noted that man-made artefacts present in the images – other than those possibly needed for calibration of the images afterwards – may introduce difficulties to the analysis. If possible, the camera should be set up so that as few foreign objects as possible are visible in the camera's field of view.

To illustrate the last point, I present an example of Karhukamera data obtained from on board *R/V Lance* in September 2007. I have already discussed this data set in chapter 4.3. This time a Karhukamera unit was mounted in the crow's nest of the ship, at the height of approximately 20 metres, looking to the fore. No man-made objects were visible in the field of view, just water and ice. Figure 43 shows an example of this kind of data.

The same classification approach, that I have deemed reasonably successful with the *Tara* data set, works even better for the *R/V Lance* data: smaller detail is being detected, and on the whole, the classified image compares more favourably with the original image. For example, practically no pixels from the middle of the ice floes are classified as water, and when there are small areas classified as ice in the water, a comparison with the original image shows that there indeed are small parcels of ice floating just at the spot.

**Figure 43**: *A Karhukamera image obtained from on board* R/V Lance.

Figure 44 shows the same image after classification. The images are not geometrically corrected; they only serve as an example of the method.

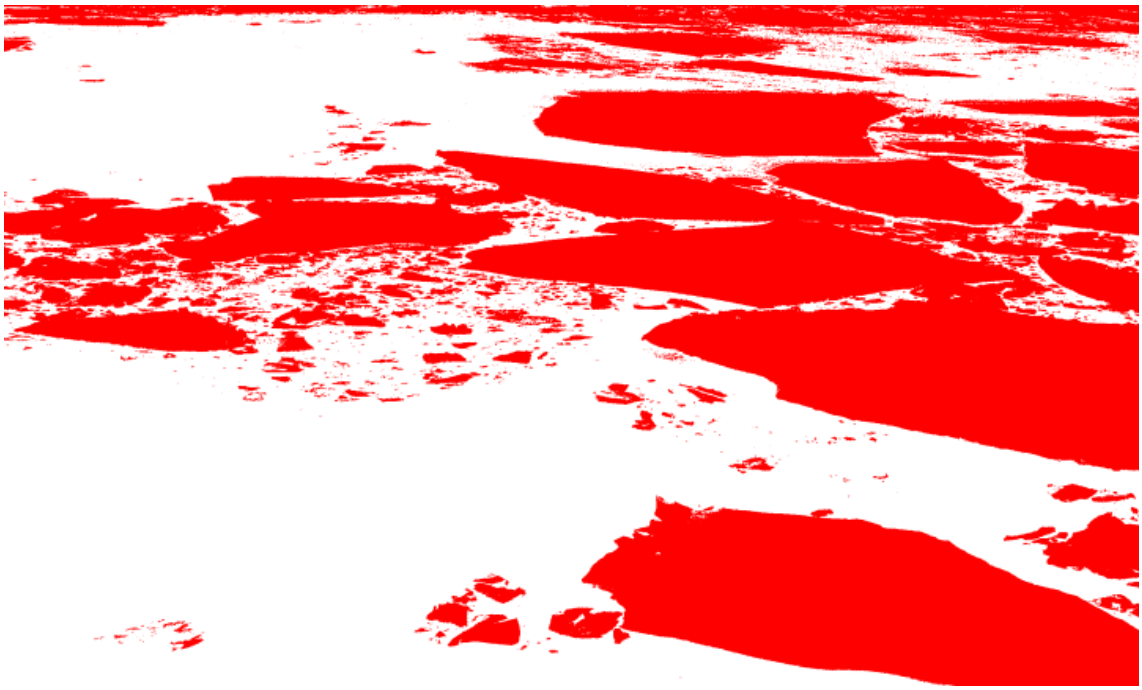

**Figure 44**: *The previous image classified as ice and water.*

Although the Karhukamera data used in this study may not be ideal, I believe that the methods I have applied are not faulty, and that a camera unit like the one used on board *Tara* may well be useful in other campaigns. The *R/V Lance* data set could be used for calculating ice concentrations, for example. That is no longer a subject of this thesis, however; it only shows that time-lapse photography is indeed a tool suited for sea ice research.

# Acknowledgments

My thesis would not be finished at all, let alone in time, without help. I'm grateful for Jari Haapala and Seppo Manninen for agreeing to be my supervisors on such short notice. Jari gave me a room to shut myself into, a cranky computer, and his presence next door, always ready and willing to help. All were much appreciated.

I'd also like to thank István Heiler for his untiring support and creativity in image correction matters, and Seppo Kaitala for kindly introducing me to GRASS. Karhukamera project gave me the idea for this research and the data to work on. I'm thankful for all Karhukamera people, especially Mikko Viitapohja. I'm also grateful for Marcel Nicolaus for providing the DAMOCLES snow depth data.

I owe thanks to Eero Rinne in his professional person, for providing me with many useful comments and technical support along the way. But most of all I'm thankful for Eero Rinne in his private person, for being a kind and supportive partner above and beyond the call of duty; in short, for making life sweet. This thesis is dedicated to Eero and the duckies, with love.

# References

## *Printed references*

Curry, Judith A., Julie L. Schramm & Elizabeth E. Ebert, 1995. Sea ice–albedo climate feedback mechanism. *Journal of Climate, 8*, 240–247.

Curry, J. A., J. L. Schramm, D. K. Perovich & J. O. Pinto, 2001. Applications of SHEBA/FIRE data to evaluation of snow/ice albedo parameterizations. *Journal of Geophysical research, 106 (D14)*, 15,345–15,355.

Derksen, C., J. Piwowar & E. LeDrew, 1997. Sea-ice melt pond fraction as determined from low lever aerial photographs. *Arctic and Alpine Research, 29(3)*, 345–351.

Eicken, H., R. Gradinger, B. Ivanov, A. Makshtas & R. Pác, 1994. Surface melt puddles on multi-year sea ice in the Eurasian Arctic. In *Proceedings of the ACSYS Conference on the Dynamics of the Arctic Climate System (WCRP-94),* Göteborg, Sweden, 267–271.

El Naggar, S., C. Garrity & R. O. Ramseier, 1998. The modelling of sea ice melt-water ponds for the High Arctic using an airborne line scan camera, and applied to the Satellite Special Sensor Microwave/Imager (SSM/I). *International Journal of Remote Sensing, 19 (12),* 2372–2394.

Fetterer, Florence & Norbert Untersteiner, 1998. Observations of melt ponds on Arctic sea ice. *Journal of Geophysical Research, 103 (C11)*, 24,821–24,835.

Gascard, J.-C., J. Festy, H. le Goff, M. Weber, B. Bruemmer, M. Offermann, M. Doble, P. Wadhams, R. Forsberg, S. Hanson, H. Skourup, S. Gerland, M. Nicolaus, J.-P- Metaxian, J. Grangeon, J. Haapala, E. Rinne, C. Haas, G. Heygster, E. Jakobson, T. Palo, J. Wilkinson, L. Kaleschke, K. Claffey. B. Elder & J. Bottenheim, 2008. Exploring Arctic Transpolar Drift During Dramatic Sea Ice Retreat. *Eos, 89 (3)*, 21–28.

Grenfell, Thomas C. & Gary A. Maykut, 1977. The Optical properties of ice and snow in the Arctic Basin. *Journal of Glaciology, 18 (80)*, 445–463.

Hanson, Kirby J., 1961. The albedo of sea ice and ice islands in the Arctic Ocean basin. *Arctic, 14*, 188–196.

Langleben, M. P., 1969. Albedo and degree of puddling of a melting cover of sea ice. *Journal of Glaciology, 8 (54)*, 407–412.

Langleben, M. P., 1971. Albedo of melting sea ice in the Southern Beaufort Sea. *Journal of Glaciology, 10 (58)*, 101–104.

Maykut, Gary A., 1986. The surface heat and mass balance. In Untersteiner, Norbert: *The Geophysics of Sea Ice.* NATO ASI Series, Series B: Physics (146). Plenum Press, New York & London, 395–463.

Myrberg, Kai, Matti Leppäranta & Harri Kuosa, 2006. *Itämeren fysiikka, tila ja tulevaisuus*. Yliopistopaino / Helsinki University Press, Helsinki.

Neteler, Markus & Helena Mitasova, 2002. *Open Source GIS: A GRASS GIS Approach.* Kluwer Academic Publishers, Norwell, Massachusetts.

Perovich, Donald K. & Walter B. Tucker III, 1997. Arctic sea-ice conditions and the distribution of solar radiation during summer. *Annals of Glaciology, 25*, 445–450.

Perovich, Donald K., Collin S. Roesler & W. Scott Pegau, 1998. Variability in Arctic sea ice optical properties. *Journal of Geophysical Research, 103 (C1)*, 1193–1208.

Perovich, Donald K., 1998. The Optical properties of sea ice. In Leppäranta, Matti (ed.): *Physics of Ice-Covered Seas. Lecture notes from a summer school in Savonlinna, Finland, 6−17 June 1994.* University of Helsinki, Helsinki, 195−230.

Perovich, D. K., W. B. Tucker III & K. A. Ligett, 2002a. Aerial observations of the evolution of ice surface conditions during summer. *Journal of Geophysical Research 107 (C10)*, SHE 24 (1–14).

Perovich, D. K., T. C. Grenfell, B. Light & P. V. Hobbs, 2002b. Seasonal evolution of the albedo of multiyear Arctic sea ice. *Journal of Geophysical Research, 107 (C10)*, SHE 20 (1–13).

Thomas, David N. & Gerhard S. Dieckmann, 2003. *Sea Ice: An Introduction to its Physics, Chemistry, Biology and Geology*. Blackwell Science, Oxford, UK.

Tschudi, Mark A., Judith A. Curry & James A. Maslanik, 1997. Determination of areal surface-featured coverage in the Beaufort Sea using aircraft video data. *Annals of Glaciology, 25*, 434-438.

Tschudi, Mark A., J. A. Curry & J. A. Maslanik, 2001. Airborne observations of summertime surface features and their effect on surface albedo during FIRE/SHEBA. *Journal of Geophysical Research 106 (D14)*, 15,335–15,344.

Tucker, W. B., A. J. Gow, D. A. Meese & H. W. Bosworth, 1999. Physical characteristics of summer sea ice across the Arctic Ocean. *Journal of Geophysical Research 104 (C1),* 1489–1504.

Untersteiner, Norbert, 1986. *The Geophysics of Sea Ice.* Plenum Press, New York.

Wadhams, Peter, 2000. *Ice in the Ocean.* Gordon and Breach Science Publishers, Australia, Canada etc.

Wadhams, Peter, 2006. Arctic sea ice thickness – a review of current techniques and future possibilities. In A*rctic Sea Ice Thickness: Past, Present & Future. International Workshop, Rungstedgaard, Denmark 8–9 November 2005.* European Commission, Brussels, 12–21.

## *Unprinted references*

Automatic Ice Cameras home page: http://icecams.org

Döscher, Ralf, Michael Karcher & Frank Kauker: Arctic sea ice in IPCC climate scenarios in view of the 2007 record low sea ice event. Published at DAMOCLES home page (http://www.damocles-eu.org), saved 31.3.2008.

Karhukamera project home page: http://www.karhukamera.com

Landmark, Bjørn, Øystein B. Dick & Kjell Kloster, 1995. *Earth Observation.* A compendium for course AGF-207: Space Activities / Earth Observation at the University Centre on Svalbard (UNIS).

Leisti, Hanna, 2007. *Compression in the Sea Ice Field*. Master's Thesis, University of Helsinki, Department of Physical Sciences, Division of Geophysics, Helsinki.